1   Revision 1

2

3   **A novel protocol for resolving feldspar crystals in synchrotron X-ray microtomographic**

4   **images of crystallized natural magmas and synthetic analogues**

5

6   Arzilli Fabio[abc*], Polacci Margherita[bc], Landi Patrizia[c], Giordano Daniele[d], Baker Don R.[e] and

7   Mancini Lucia[a]

8

9   [a]Elettra-Sincrotrone Trieste S.C.p.A., SS 14, Km 163.5 in Area Science Park, 34149 Basovizza

10   (Trieste), Italy

11   [b]School of Earth, Atmospheric and Environmental Sciences, University of Manchester, Oxford

12   Road, Manchester, M13 9PL, UK

13   [c]Istituto Nazionale di Geofisica e Vulcanologia, sezione di Pisa, via della Faggiola 32, 56126 Pisa,

14   Italy

15   [d]Dipartimento di Scienze della Terra, Università di Torino, Via Valperga Caluso 35,10125 Torino,

16   Italy

17   [e]Department of Earth and Planetary Sciences, McGill University, H3A 0E8 Quebec, Canada

18

19

20   [*]Corresponding author: Fabio Arzilli

21   Corresponding author present affiliation: School of Earth, Atmospheric and Environmental

22   Sciences, University of Manchester, Oxford Road, Manchester, M13 9PL, UK

23   E-mail address: arzilli.fabio@gmail.com

24   mobile: +393298429732; +447904104670

25

1

26   **ABSTRACT**

27   X-ray computed microtomography is a non-destructive imaging technique recognized in the

28   geosciences as a powerful tool to investigate rock textures directly in three dimensions (3D) at the

29   micron and sub-micron scale. The quantitative morphological and textural analysis of images

30   requires segmentation and characterization of phases in the reconstructed volume based upon their

31   gray levels (related to their relative X-ray attenuation) and/or morphological aspects. Often the

32   differences in X-ray attenuation of some phases are so small that no contrast is observed in the

33   reconstructed slices or, although the human eye can discern the differences between these phases, it

34   is difficult, or sometimes impossible, to reliably segment and separately analyze these phases.

35   Facing this challenge, we propose an experimental and computational procedure that allows the

36   segmentation of phases with small density variations in geomaterials. By using an experimental

37   protocol based on phase-contrast synchrotron X-ray microtomography combined with a customized

38   3D image processing procedure, we successfully segmented feldspar from the glassy matrix in both

39   a natural volcanic sample and a synthetic analogue. Our results demonstrate that crystallized natural

40   volcanic rocks and synthetic analogues can be characterized by synchrotron X-ray phase-contrast

41   microtomography and that phase-retrieval processing is an invaluable tool for the reconstruction of

42   3D multiphase textures.

43

44

45

46

49

50

2

INTRODUCTION

Overview on textural analysis of crystallized rocks with focus on feldspar crystals

The study of rock textures is important to understand the evolution of the conditions and processes that lead to their formation. Crystal abundances, sizes, shapes and spatial distributions represent specific markers of the paragenesis of magmas during transport in the crust towards the surface and give us information on the time scales of magma ascent (Marsh 1988, 1998; Higgins 2000, 2002, 2006; Hersum and Marsh 2007; Marsh 2007; Baker et al. 2012a). Crystal and vesicle textures are conventionally studied using optical and Scanning Electron Microscopy (SEM), which only allow two-dimensional (2D) imaging of samples. In recent years, three-dimensional (3D) analysis of rock textures, using X-ray and neutron computed microtomography (µCT), has become a fundamental tool to investigate their properties (e.g. porosity, crystallinity, crystal and vesicle size distributions, shapes, orientations, connectivity, etc.) through a non-destructive, volumetric characterization (Fig. 1). X-ray µCT allows us to image larger sample volumes (from mm-sized volumes with spatial resolutions at the sub-micron and micron scale up to several tens of mm volumes working at spatial resolutions of the order of 40-50 microns) than a thin section (with a typical size of 27 x 46 x 0.030 mm^3). X-ray µCT provides a realistic visualization of the 3D shapes and orientations of crystals that can be quantified through the extraction of parameters such as volume fraction, size distributions, orientation, connectivity, etc. A great advantage of 3D imaging and analysis is that it does not require any stereological corrections as in the 2D approach (Fig. 1). Moreover, no specific sample preparation is required before X-ray imaging analysis. However, like all techniques, X-ray µCT has limitations, and for some studies detailed analysis of 2D sections provides complementary data that cannot be easily obtained from using X-ray µ-CT only (Baker et al. 2012a). High resolution SEM images can be used to segment and separate tiny crystals (<1 µm) over large areas (typically ca. 0.5 mm x 0.5 mm^2) of the sample (Fig. 1). This approach is often complementary to X-ray µCT to characterize different aspects of the same process, such as the

3

76 nucleation and twinning of crystals (e.g., Arzilli et al. 2015). Back-scattered SEM images allow us

77 to distinguish phases with similar average atomic number (e.g., feldspars and trachytic glass) and

78 chemical information can be also obtained. Furthermore, the ease of access to an SEM is

79 advantageous when compared to synchrotron facilities (Baker et al. 2012a).

80 X-ray μCT has been successfully employed for the 3D study of the textures of igneous,

81 metamorphic and sedimentary rocks (e.g., Carlson 2006; Polacci et al. 2009; Baker et al. 2012a;

82 Madonna et al. 2013; Cnudde and Boone 2013; Cilona et al. 2014; Fusseis et al. 2014; Zucali et al.

83 2014a,b). This technique has been used to characterize the occurrence and evolution of vesiculation

84 and crystallization recorded in different types of natural igneous and metamorphic rocks (e.g.,

85 Carlson and Denison 1992; Zandomeneghi et al. 2010; Degruyter et al. 2010a,b; Voltolini et al.

86 2011; Baker et al. 2012b; Pamukcu et al. 2012; Polacci et al. 2012). In particular, through this

87 technique, several authors have investigated i) the crystallization and fabric of metamorphic rocks

88 (Carlson and Denison 1992; Carlson et al. 1995; Denison and Carlson 1997; Brown et al. 1999;

89 Ketcham and Carlson 2001; Carlson 2002; Ketcham 2005; Ketcham et al. 2005; Zucali et al. 2014;

90 Sayab et al. 2014); ii) silicate and oxide crystals dispersed in a glassy matrix of volcanic pumices

91 and scoriae (e.g., Gualda 2006; Gualda and Rivers 2006; Pamukcu and Gualda 2010; Gualda et al.

92 2010; Zandomeneghi et al. 2010; Voltolini et al. 2011; Pamukcu et al. 2012); iii) kimberlite

93 textures, by segmenting olivine phenocrysts from an altered clay-rich matrix (Jerram et al. 2009);

94 iv) oxide and sulfide minerals associated with magmatic ore deposits (Godel et al. 2010; Barnes et

95 al. 2011; Godel et al. 2012; Godel et al. 2013, 2014); the texture of meteorites, regolith particles and

96 chondrules, by segmenting Fe–Ni alloy and sulfide grains dispersed in a silicate matrix (Benedix et

97 al. 2008; Ebel et al. 2008; Friedrich et al. 2008; Uesugi et al. 2010; Tsuchiyama et al. 2011; Uesugi

98 et al. 2013; Tsuchiyama et al. 2013).

99 This comprehensive, although non-exhaustive, list demonstrates that in the last 20 years a

100 growing use of X-ray μCT has occurred in the analysis of crystallized rock textures resulting in

4

101 scientific and technological advancements in the capability of visualizing and characterizing rock-

102 forming phases in 3D. However, distinguishing different crystalline phases with small variations of

103 the attenuation coefficients still represent a challenge in X-ray imaging, both from an analytical and

104 computational point of view.

105   In volcanic rock samples, vesicles are more easily resolved from the other phases in the rock

106 (crystals and glass) because of their significantly lower X-ray attenuation. On the other hand,

107 distinguishing amongst different types of ferromagnesian crystals (e.g., pyroxenes and olivine) and

108 types of feldspars (plagioclase and alkali feldspars) is challenging because their X-ray attenuation

109 coefficients are similar. Furthermore, in X-ray image processing feldspar is one of the most difficult

110 phases to segment from the glassy matrix (e.g., Giachetti et al. 2011) (Fig. 2), and only a few

111 studies have addressed the separation of feldspar from the matrix using a 3D approach (e.g.,

112 Zandomeneghi et al. 2010; Voltolini et al. 2011; Arzilli et al. 2015).

113   In recent years, a growing literature devoted to the establishment of sophisticated strategies to

114 solve the problem of separation of mineral phases with similar densities in igneous rocks has been

115 published (Uesugi et al. 1999; Tsuchiyama et al. 2000; Ketcham and Carlson 2001; Gualda and

116 Rivers 2006; Pamukcu and Gualda 2010; Zandomenegi et al. 2010; Voltolini et al. 2011; Pamukcu

117 et al. 2012). One solution to this challenge is the "dual-energy X-ray microtomography" technique,

118 which exploits the different absorption of materials at two different X-ray energies. With this

119 approach, an X-ray μCT scan of a given sample is performed at energies above and below the X-ray

120 absorption edge of an element characteristic of the phase to be investigated. These two images are

121 then logarithmically subtracted to provide more X-ray contrast between two phases with similar

122 absorption properties (e.g., Gualda et al. 2010; Tsuchiyama et al. 2013). However, data collection

123 requires twice as much time as a single tomogram, and there are limitations in the application of this

124 technique to major minerals of volcanic rocks, even though it is suitable for accessory minerals such

125 as magnetite, titanite, zircon and allanite (Gualda et al. 2010). This method is potentially applicable

5

126   to rock samples crystallized under equilibrium conditions (Gualda et al. 2010; Tsuchiyama et al.

127   2013). However, a further limitation of such method is related to rocks that are not in equilibrium in

128   the system, such as volcanic rocks or experimental samples. In these samples, in fact, there is a

129   great risk for overlapping X-ray attenuation coefficients among phases because the chemical

130   zonation present in these minerals expands the range of X-ray attenuation coefficients.

131

132   **Motivation for the study**

133   We developed an experimental and computational procedure that can be applied to X-ray μCT

134   images to segment and analyze phases with similar X-ray attenuation coefficients in geological

135   specimen. We illustrate the proposed procedure using feldspar crystals and silicate glass as example

136   of geomaterials because of the ubiquity of feldspar crystals in igneous rocks and the challenge

137   represented by segmentation and separation of this phase in X-ray image processing.

138   Two samples were selected as test cases (Table 1), each containing two phases with similar X-

139   ray attenuation coefficients that makes phase separation and segmentation via commonly used

140   experimental protocols impossible (Zandomeneghi et al. 2010; Baker al. 2012a). The first sample

141   was a natural pumice (sample ST164241198B) from Stromboli volcano erupted during a

142   paroxysmal explosion on the 24th of November 1998. This highly vesiculated pumice contains

143   plagioclase crystals from several hundred μm to a few mm in size, set in a basaltic glassy matrix,

144   and surrounded by a thin layer of glass and often directly in contact with vesicles (Bertagnini et al.

145   1999). In this case, labradoritic plagioclase crystals and basaltic glass have similar X-ray

146   attenuation coefficients. The second sample was a synthetic trachyte (sample D1) obtained through

147   high temperature, high pressure crystallization experiments (Arzilli and Carroll 2013), resembling

148   the composition of the magma erupted during the Campanian Ignimbrite eruption (Campi Flegrei,

149   Italy), and containing alkali feldspar crystals in the glass. The sample texture is characterized by

150   spherulitic alkali feldspar grown in a poorly vesiculated trachytic melt, with sizes ranging between a

6

151   few and hundred μm. Spherulitic crystal shapes are characterized by interstitial glass between each

152   lamella in spherulite. Such a complex texture makes the separation of alkali feldspars from the

153   surrounding rock matrix particularly difficult. In this case, the similarity of alkali feldspar (sanidine)

154   and trachytic glass X-ray attenuation coefficients (Fig. 2) makes segmentation of these crystals a

155   challenge in X-ray μCT imaging.

156

157   **METHODS**

158   **Phase-contrast μCT technique and phase-retrieval method**

159   Transmission (or absorption) X-ray μCT yields a 3D map of the linear X-ray attenuation

160   coefficient, which is a function of the atomic number and volumetric mass density of the material.

161   Based on the compositional contrasts and X-ray properties of different phases, various minerals can

162   be identified in a rock. The absorption contrast between phases in a sample is determined by

163   variations in mass density and chemical composition for a given mineral and is based exclusively

164   on the detection of amplitude variations of the transmitted X-rays. The use of phase-sensitive

165   techniques allow us to increase the dynamic range measurable by detecting contrast related to the

166   X-ray phase shifts produced by the sample in the transmitted X-ray beam. In this case, the contrast

167   will be related to the refraction of X-rays in the regions of the sample where contact between two

168   phases occurs. The contrast on the images will be a combination of absorption and refraction

169   effects; the use of phase-contrast enhances the visibility of objects with similar linear attenuation

170   coefficients by increasing the visibility of their phase boundaries (edge enhancement) (Snigerev et

171   al. 1995; Cloetens et al. 1996). The use of phase-contrast μCT requires a high spatial coherence X-

172   ray beam that is available at third generation synchrotron X-ray imaging beamlines due to the large

173   source-to-sample distance and small angular source size (Cloetens et al. 1997; Fitzgerald 2000). In

174   this case, the implementation of the technique, known as Free-Space Propagation (FSP), is very

175   simple from an experimental point of view: in order to record phase effects it is sufficient to move

7

176   the detector to a specific distance from the sample (Cloetens et al., 1996). This distance gives the

177   phase introduced by the sample the possibility to develop into intensity variations (phase contrast).

178   If the propagation distance is chosen properly, phase-contrast will result in edge enhancement.

179   Limited phase-contrast effects can also be observed and successfully exploited using a conventional

180   microfocus X-ray source in FSP mode (Wilkins et al. 1996). Phase-contrast X-ray μCT has been

181   successfully applied not only to the study of light materials (e.g., biological tissues, polymers,

182   wood) but also to the characterization of heavy materials as metallic alloys, magnetic materials

183   (e.g., Cloetens et al. 1997; Mancini et al. 1998, Baruchel et al. 2000), geomaterials (e.g., Polacci et

184   al. 2006; Marinoni et al., 2009; Zandomeneghi et al. 2010; Mayo et al. 2012; Baker et al. 2012a;

185   Fusseis et al. 2014) and to archaeological and paleonthological studies (e.g., Tafforeau et al. 2006;

186   Bernardini et al., 2012; Zanolli et al., 2014). Synchrotron X-ray phase-contrast μCT technique

187   based on free-space propagation was used in this study to discriminate among different phases in

188   the investigated rock samples.

189   Often the segmentation of phases cannot be obtained directly from the reconstructed

190   microtomographic images because of their low contrast even though they are perceptible by the

191   human eye. The cases where no contrast can be observed are even worse. As a consequence, the

192   application of phase-retrieval methods (Gureyev et al. 2006; Pfeiffer et al. 2006; Guigay et al. 2007;

193   Gureyev et al. 2008; Beltran et al. 2010; Weitkamp et al. 2011) is needed for extracting these

194   phases.

195   Phase retrieval is a technique for extracting quantitative phase information from X-ray

196   propagation-based, phase-contrast tomographic images (Cloetens et al., 1997). Phase-retrieval

197   procedures are widely used in biomedical applications (e.g., Langer et al. 2010; Mohammadi et al.

198   2014; Maire and Withers 2014), materials science (e.g. Cloetens et al., 1999; Buffière et al. 1999;

199   Mayo et al. 2012; Maire and Withers 2014) and paleontological studies (e.g., Tafforeau et al. 2006;

200   Smith et al. 2010), whereas their use in petrology and mineralogy is still very limited. Different

201   procedures have been developed to extract phase information from phase-contrast X-ray images.

202   Some approaches require recording multiple CT scans at different sample-to-detector distances

203   (e.g., holotomography; Cloetens et al., 1997), while others use phase-retrieval algorithms that are

204   based on intensity-only measurements (Teague 1983; Gureyev and Nugent 1996, 1997; Paganin and

205   Nugent 1998; Cloetens et al. 1999; Guigay et al. 2007).

206   Recently, rather than imaging samples at multiple distances from the detector, which is time

207   consuming from an experimental and computational point of view, single-distance phase-retrieval

208   algorithms have been developed. The most widely used is based on the Transfer of Intensity

209   Equation (TIE). It was introduced by Paganin et al. (2002) and it only requires the acquisition of

210   one X-ray µCT data set at a single sample-to-detector distance. The method requires *a priori*

211   knowledge of the complex refractive index (n) for each material present in the sample (Paganin et

212   al. 2002; Beltran et al. 2010). The refractive index of any given material can be expressed as:

213 $n = 1 - \delta + i\beta$

214   where δ is the refractive index (speed of light of a given wavelength in the material divided by

215   speed of that light in vacuum or air) decrement and β is the absorption index. Both the real part, δ,

216   and the imaginary part, β, are positive and dimensionless real numbers, the imaginary part β

217   describing the absorption while the real part δ describes the phase shift introduced by the material

218   (Born and Wolf, 1959; Wilkins et al., 1995; Snigerev et al., 1995; Cloetens et al., 1996). In the

219   following, we will illustrate the application of the Paganin's phase-retrieval method to the X-ray

220   images of our samples and discuss the results obtained from crystal segmentation.

221   We specify that this application of the Paganin's method did not allow us to obtain a quantitative

222   reconstruction of the mass and electron densities of the different phases present in the rock sample;

223   however, it allowed us to properly segment and characterize the phases of interest from a

224   morphological and textural point of view. Paganin's method is formally limited to homogeneous

225   objects, e.g., samples that consist of one material and air, but, in practice, it is used for multi-

9

226   material samples as well. Therefore, in these materials artifacts may appear. The artifacts consist of

227   blurring if the ratio $\gamma = \delta/\beta$ is higher than the value chosen in the reconstruction procedure. The

228   method is used despite these artifacts, because multi-phase objects are described by a more-

229   complicated relationship between absorption and phase. In fact, to properly characterize multi-

230   material objects requires more than one image at each tomographic angle for proper phase retrieval

231   (Burvall et al. 2011), a method too time-consuming and expensive for routine X-ray μCT.

232

233   **Synchrotron phase-contrast X-ray μCT measurements**

234   Synchrotron phase-contrast X-ray μCT measurements were performed at the SYRMEP beamline

235   (Tromba et al. 2010) of the Elettra - Sincrotrone Trieste laboratory (Basovizza, Italy). Elettra is a

236   third generation synchrotron facility, and the SYRMEP beamline, devoted to the application of hard

237   X-ray imaging techniques, operates in an energy range between 8.5 and 38 keV. The experiments

238   were performed in white-beam mode, which at SYRMEP provides a nearly parallel, laminar-shaped

239   X-ray beam with a maximum area of 100 mm (horizontal) x 6 mm (vertical) at 15 m from the

240   source. An air-cooled, 16 bit microscope CCD camera with a 2048 x 2048 pixel chip (KAI 4022M

241   CCD, Photonic Science) was used to acquire the μCT scans (Figs 3a and 4a). The optical system is

242   based on the indirect detection of X-rays: a 25 μm thick single crystal LuAG:Ce scintillator screen,

243   used to convert X-rays into visible light, was lens-coupled to the CCD camera. The sample-to-

244   detector distance was set to 150 mm. For each sample 1800 radiographic images (or projections)

245   were acquired by the detector with equiangular steps over a full rotation angle of 180° and an

246   exposure time/projection of 2.1 seconds.

247

248   **IMAGE PROCESSING AND RESULTS**

249   **Slice reconstruction and segmentation**

250   The Syrmep_tomo_project 4.0 software, custom-developed at the SYRMEP beamline, and the

251   GRIDREC algorithm (Dowd et al. 1987) were used to reconstruct the 2D axial slices from the

252   sample projections. These slices were then converted to the 8-bit raw format and stacked by using

253   the *Fiji* software (Schneider et al. 2012) to obtain volumes in which the isotropic voxel has an edge

254   size of 2.2 μm for the Stromboli pumice and 2 μm for the synthetic trachytic sample. 3D

255   visualization (volume rendering) of the reconstructed volumes was obtained with the commercial

256   software VGStudio MAX 2.0 (Volume Graphics).

257   Prior to segmentation, a Volume of Interest (VOI) was selected for both investigated samples.

258   For the Stromboli pumice, the VOI corresponds roughly to the whole imaged volume (Table 1), the

259   external part of which was cropped close to the outer boundaries of the sample. The synthetic

260   trachyte VOI coincided with the whole sample (Table 1) (Arzilli et al. 2015).

261   The reconstructed slices of the Stromboli pumice (Fig. 3a) show a low contrast between

262   plagioclase, vesicles and basaltic glass, which is why after the application of manual thresholding

263   the Stromboli pumice binary images appear very noisy (Fig. 3b). The segmentation of alkali

264   feldspars in the synthetic sample was impossible because the contrast of this mineral is too close to

265   that of the glass (Fig. 4a). Therefore, in both samples the segmentation process required a pre-

266   processing step, which consisted in applying phase-retrieval processing in order to enhance the

267   contrast between plagioclase and alkali feldspar and the glassy matrix (Figs 3 and 4).

268   To achieve this objective the single-distance phase-retrieval algorithm developed by Paganin et

269   al. (2002) was applied to the acquired radiographic images to allow segmentation of crystals from

270   silicate glass. This algorithm combined with the Filtered Back-Projection algorithm (Herman 1980)

271   was used to reconstruct the 3D distribution of the complex X-ray refractive index within the sample.

272   This processing was performed using the commercial software package X-TRACT (Paganin et al.

273   2002; Mohammadi et al. 2014), version 5.8, developed by the CSIRO group

274   (http://xrsi.cmit.csiro.au/WebHelp/X-TRACT/webframe.html, Canberra, Australia) (Fig. 5a),

11

275   although alternative freeware solutions to the application of the Paganin's algorithm and

276   synchrotron X-ray CT reconstruction could have been used (Weitkamp et al. 2011; Chen et al.

277   2012; Rivers 2012; Gursoy et al. 2014; Brun et al. 2015).

278   The ratio γ between the real and imaginary part of the refractive index is constant at a given

279   wavelength for a homogeneous material. We calculated the δ and β values using the freeware from

280   the Center for X-ray Optics database (http://henke.lbl.gov/optical_constants/getdb2.html) (Henke et

281   al. 1993). The refractive index can be obtained from the chemical formula of the phase of interest,

282   its mass density (g/cm^3) and the photon energy (keV) used during the X-ray μCT acquisition (Figs.

283   5 and 6). In white beam mode, the energy selection was done considering the medium energy of the

284   spectrum employed during the experiment (22 keV)**.** The mass density of feldspar was obtained

285   from the Mindat website (http://www.mindat.org; Ralph and Chau, 2014): the density of labradorite

286   (2.69 g/cm^3) was used for the Stromboli plagioclase crystals, and the density of sanidine (2.52

287   g/cm^3) was used for the synthetic trachyte alkali feldspar. Figure 6 shows the variation of γ as a

288   function of the photon energy. The calculated γ value for plagioclase (labradorite) in the natural

289   Stromboli pumice is 353, whereas, for alkali feldspar (sanidine) in the synthetic sample γ is 362.

290   The initially calculated γ values (Fig. 6) did not sufficiently increase the contrast among phases.

291   In order to enhance contrast these values were tuned by visual inspection to achieve two results: i)

292   reduction of phase-contrast "artifacts" at the edges of the crystals and ii) enhancement of contrast

293   between feldspars and glass. Unfortunately, blurring of the images is generally a consequence of the

294   application of the TIE phase-retrieval algorithm. Therefore, for each data set a few iterations were

295   needed in order to optimize the γ parameter to obtain the best contrast while minimizing blurring

296   effects. The initial γ value for plagioclase (labradorite) in the natural Stromboli pumice was then

297   tuned to $\gamma = 120$. The same procedure was applied to alkali feldspar (sanidine) in the synthetic

298   sample, tuning the γ value to 50 (Arzilli et al. 2015). The final results of this procedure strongly

299 enhance the contrast between plagioclase crystals, vesicles and glass in the natural pumice (Figs 7b

300 and 8a). These images can be compared to the results of reconstruction without phase-retrieval

301 processing presented in Figs 3a and 7a. A similar increase in contrast was obtained for the alkali

302 feldspars and trachytic glass in the synthetic sample (Figs 4b and 7c-d).

303 After phase retrieval, the reconstructed slices of the Stromboli pumice sample were corrupted by

304 artifacts with the appearance of concentric rings and named 'ring artifacts' in CT imaging (Fig. 7b).

305 These artifacts may arise in synchrotron radiation μCT from dead pixels in CCD detectors,

306 damaged scintillator screens and instabilities of the synchrotron beam (Rivers 1998; Titarenko et al.

307 2010; Van Nieuwenhove 2015). The version of the X-TRACT software we used in this work

308 allowed us to only apply a ring-removing filter developed by Rivers (1998) that is based on

309 sinogram-processing. In our study, the Rivers's filter was insufficient to remove all ring artifacts in

310 the data set. However, because the majority of plagioclase crystals were not corrupted by rings this

311 allowed us to correctly perform their segmentation. In more complicated cases, other filters may

312 need to be applied to reduce ring artifacts during the reconstruction procedure (e.g. Sijbers and

313 Postonov 2004; Münch et al. 2009). Some freeware for CT reconstruction (Marone et al. 2010;

314 Chen et al. 2012; Gursoy et al. 2014, Brun et al. 2015) allows the application of these filters for ring

315 artifact reduction.

316

317 **Segmentation of plagioclase crystals in the natural Stromboli pumice**

318 The next step in image processing was segmentation. This process allows the separation of

319 objects from the background to obtain binary volumes containing only the feature of interest.

320 Several segmentation techniques are available, but there is no single method successfully applicable

321 to all cases and the procedure is sample-dependent. Segmentation was performed with the *Pore3D*

322 software library (Brun et al. 2010). To this purpose, we applied a manual bi-level thresholding in

323 3D that allowed us to segment the features of interest from the background by selecting a threshold

13

324 value (Pal and Pal 1993) based on the analysis of the histogram of gray levels in the VOI (selecting

325 the threshold in the region near two peaks). The oscillatory compositional zoning of the plagioclase

326 phenocrysts in the Stromboli samples was not resolvable using phase-contrast X-ray μCT.

327 Therefore, using the phase-retrieval procedure we assumed a homogeneous plagioclase crystal

328 density. Plagioclase crystals were separated from vesicles and glass through segmentation combined

329 with a masking procedure based on plagioclase shape (Faessel and Jeulin 2010; Lin et al. 2015).

330 The image background of our Stromboli pumice was affected by Poisson noise, which consists

331 of random variations in brightness levels that can corrupt the image quality (Lev et al. 1977; Le et

332 al. 2007). Because of the inherent resolution limitations of the X-ray μCT technique, images were

333 also affected by partial-volume effects (Ketcham 2005), which consist of variations in attenuation

334 shown by each pixel and result in a blurring of material boundaries (the material in any one voxel

335 can affect X-ray attenuation values of surrounding voxels). Variations in attenuation are due to

336 chemical zonation in plagioclase, chemical heterogeneities in the glass, and limited spatial

337 resolution. Poisson noise and partial-volume effects made the segmentation of plagioclase difficult.

338 As an example, Fig. 8b-c shows pixel outliers belonging to both vesicles and glassy matrix that

339 were not segmented after thresholding. We know there are no plagioclase crystals in vesicles, and

340 so we have an internal gauge of signal, which we then used to assess the accuracy of the rest of the

341 image.

342 Following this approach, the masking procedure consisted in segmenting plagioclase via two

343 different steps:

344 a) The first step consisted of manual bi-level thresholding, using the *Pore3D* software, in order

345 to segment the realistic shape of plagioclase crystals taking into account a significant amount of

346 pixel outliers left in the binary images (Figs 8b and 9);

347 b) The second step consisted in the approximate isolation of plagioclase trying to take into

348 account the minimum possible amount of pixel outliers (Fig. 8c) with the aim of obtaining a mask

14

349   of the plagioclase shapes (Fig. 8d). The amount of pixel outliers was partially removed using a

350   sequence of filters on the segmented, binary image. First, we used a 3D filter removing outliers with

351   the *Pore3D* software library and, subsequently, a similar 2D filter with the *Fiji* software (Fig. 9).

352   Through these filters we were able to delete connected components with volume sizes below a

353   specified threshold value based upon visual inspection (Figs. 8c-d and 9). The combined use of 3D

354   and 2D filters applied to binary images allowed us to remove most of the pixel outliers without

355   changing crystal shapes. The shapes of plagioclase crystals were isolated using 4 cycles of 2D

356   erosion and dilation filters in *Fiji*. In order to avoid excessive plagioclase shape change when

357   applying the erosion filter, the internal voids of plagioclase crystals were filled during the masking

358   process, which also produced crystals that are more compact. Through the second step of

359   segmentation, a mask of plagioclase crystals was obtained (Figs. 8d and 9).

360   The masking operation was combined with the first segmentation by applying the logic AND

361   operator in *Fiji* (Fig. 8b-d) in order to complete the separation of the phases of interest (Figs 8e and

362   9). The plagioclase crystals were completely segmented preserving their shapes and internal

363   structures (Figs. 8e and 10a). This method had the additional benefit of reducing the effect of the

364   ring artifacts on the segmentation of plagioclase crystals. The procedure used for the Stromboli's

365   sample, including phase retrieval and segmentation, can take about 3 hours per each sample.

366

367   **Segmentation of alkali feldspar crystals in the trachytic synthetic sample**

368   In the synthetic trachyte, semi-automatic volume segmentation (Zanolli et al. 2014; Arzilli et al.

369   2015) with manual corrections was performed to separate crystals of alkali feldspar from the glassy

370   matrix by using the *AMIRA*® software v.4.1.2 (Mercury Computer Systems). Semi-automatic

371   volume segmentation with manual corrections can also be performed with the *Avizo*® *3D* software

372   (FEI Visualization Sciences Group). This segmentation consists of manually drawing the edges of

373   the crystals on the 2D slices. This is repeated every 5-10 slices (this interval depends on the size of

15

374   the crystal and the complexity of their shape) from the beginning to the end of the crystal, while in

375   the intermediate slices the crystal shape will be reconstructed automatically by the software (via an

376   interpolation procedure). The advantage of this technique is that the operator can obtain the real

377   morphology of the object of interest by visual inspection (Fig. 10b). This technique can be time

378   consuming for a large numbers of crystals, but it is a valuable approach in specific cases related to

379   the study of crystal nucleation, twinning and crystal lattice orientation (Arzilli et al. 2015).

380

381   **IMPLICATIONS**

382   **Success of the procedure**

383   In this work, we used for the first time a single-distance phase-retrieval method to successfully

384   resolve feldspar crystals in a glassy rock matrix. More specifically, this method allowed us to

385   display the habits and spatial distribution of plagioclase crystals in a natural pumice of Stromboli

386   (Fig. 10a) and to display shapes and orientation of alkali feldspar in a synthetic trachytic glass (Fig.

387   10b). Both these results would have been impossible to obtain if not for the application of our

388   newly developed protocol.

389   The segmentation approach adopted for the Stromboli pumice is an invaluable tool for

390   petrologists and volcanologists to quantify, for instance, crystal volume fractions and crystal

391   number densities. On the other hand, the combination of phase-retrieval procedures and semi-

392   automatic volume segmentation used for the synthetic sample represents a powerful tool for

393   mineralogists and petrologists to investigate crystallographic orientations and crystal nucleation

394   processes.

395   Recently, several authors have discussed the effect of X-rays on attenuation and transmission to

396   distinguish between different minerals and glass compositions using X-ray microtomography (e.g.,

397   Tsuchiyama et al. 2005; Gualda and Rivers 2006; Gualda et al. 2010; Baker et al. 2012a;

398   Tsuchiyama et al. 2013). The X-ray attenuation coefficient for magnetite is larger than that of

16

399   quartz, feldspar or glass, making dense minerals easily distinguishable from silicic glasses and

400   felsic minerals (Gualda and Rivers 2006; Gualda et al. 2010). Whereas the X-ray attenuation

401   coefficients for quartz and feldspar are very close to that of several silicate glasses, and

402   segmentation is very challenging (e.g., Gualda and Rivers 2006; Pamukcu et al. 2010; Voltolini et

403   al. 2011; Arzilli et al. 2015). Therefore, the main contribution of this study to petrology is to

404   propose a novel application of the phase-retrieval procedure in 3D image processing in order to

405   resolve feldspar crystals in multiphase crystallized rocks. This procedure is significantly important

406   for the volcanological and petrological community because it opens new avenues in the 3D study of

407   crystallization kinetics of silicate melts, which, together with degassing, is the most important

408   process driving magma and eruption dynamics.

409   Despite the observation that the phase-retrieval method employed here has limitations, such as a

410   slight blurring of images, which in our work was kept to a minimum to avoid significant changes in

411   crystal shape, it represents a fundamental step in image processing in order to increase the contrast

412   among minerals displaying only slightly different X-ray attenuations. This means that small

413   differences in density and chemical composition can be resolved through phase-contrast imaging, as

414   already shown in paleontological specimens, materials science and biomedical applications (e.g.,

415   Tafforeau et al. 2006; Smith et al. 2010; Langer et al. 2010; Mayo et al. 2012; Mohammadi et al.

416   2014). Another limitation is the need to use a suite of software tools to execute the protocol; we

417   expect that in the near future a single software package will contain all of the algorithms necessary,

418   which will accelerate the data processing. The techniques shown here can be applied to a wide

419   range of natural rocks and synthetic samples characterized by the presence of crystals with sizes

420   between a few μm to a few mm and phases with similar X-ray attenuation coefficients.

421   The results of this study highlight that careful application of a phase-retrieval algorithm to

422   synchrotron X-ray microtomographic data sets of volcanic rocks can provide fundamental

423   information for 3D quantitative analysis of magmatic crystallization processes. We envisage that

424 future work will expand the range of application of this procedure to different geomaterials. It is

425 worth noting that our imaging protocol can be further refined (for instance using a phase-retrieval

426 approach for multi-material objects as proposed by Beltran et al. (2010)) and also applied to older

427 data sets in order to extract data that could not be extracted before.

428

429

430

439

440

441

References

443   Arzilli, F., and Carroll, M.R. (2013) Crystallization kinetics of alkali feldspars in cooling and

444 decompression-induced crystallization experiments in trachytic melt. Contribution to Mineralogy

445 and Petrology, 166, 1011-1027.

446   Arzilli, F., Mancini, L., Voltolini, M., Cicconi, M.R., Mohammadi, S., Giuli, G., Mainprice, D.,

447 Paris, E., Barou, F., and Carroll M.R. (2015) Near-liquidus growth of feldspar spherulites in

448   trachytic melts: 3D morphologies and implications in crystallization mechanisms. Lithos, 216–217,

449   93–105.

450   Baker, D.R., Mancini, L., Polacci, M., Higgins, M.D., Gualda, G.A.R., Hill, R.J., and Rivers

451   M.L. (2012a) An introduction to the application of X-ray microtomography to the three-

452   dimensional study of igneous rocks. Lithos, 148, 262-276.

453   Baker, D.R., Brun, F., O'Shaughnessy, C., Mancini, L., Fife, J.L., and Rivers, M. (2012b) A

454   four-dimensional X-ray tomographic microscopy study of bubble growth in basaltic foam. Nature

455   Communications, 3, 1135.

456   Barnes, S.J., Osborne, G., Cook, D., Barnes, L., Maier, W.D., and Godel B. (2011) The Santa

457   Rita nickel sulfide deposit in the Fazenda Mirabela Intrusion, Bahia, Brazil: geology, sulfide

458   geochemistry and genesis. Economic Geology, 106, 1083–1110.

459   Baruchel, J., Cloetens, P., Härtwig, J., Ludwig, W., Mancini, L., Pernot, P., and Schlenker M.

460   (2000) Phase imaging using highly coherent X-rays: Radiography, tomography, diffraction

461   topography. Journal of Synchrotron Radiation, 7, 196–201.

462   Beltran, M.A., Paganin, D.M., Uesugi, K., and Kitchen M.J. (2010) 2D and 3D X-ray phase

463   retrieval of multi-material objects using a single defocus distance. Optics Express, 18, 6423-6436.

464   Benedix, G.K., Ketcham, R.A., Wilson, L., McCoy, T.J., Bogard, D.D., Garrison, D.H., Herzog,

465   G.F., Xue, S., Klein, J., and Middleton R. (2008) The formation and chronology of the PAT 91501

466   impact-melt L chondrite with vesicle–metal-sulfide assemblages. Geochimica et Cosmochimica

467   Acta, 72, 2417–2428.

468   Bernardini, F., Tuniz, C., Coppa, A., Mancini, L., Dreossi, D., Eichert, D., Turco, G., Biasotto,

469   M., Terrasi, F., De Cesare, N., Hua, Q., and Levchenko V. (2012) Beeswax as Dental Filling on a

470   Neolithic Human Tooth. PLoS ONE, 7 - 9, e44904.

471   Bertagnini, A., Coltelli, M., Landi, P., Pompilio, M., and Rosi M. (1999) Violent explosions

472   yield new insights into dynamics of Stromboli volcano. Eos Transactions AGU, 80, 633–636.

473   Brun, F., Mancini, L., Kasae, P., Favretto, S., Dreossi, D., and Tromba G. (2010) Pore3D: A

474   software library for quantitative analysis of porous media. Nuclear Instruments and Methods in

475   Physics Research A, 615, 326–332.

476   Brun, F., Pacilè, S., Accardo, A., Kourousias, G., Dreossi, D., Mancini, L., Tromba, G., and

477   Pugliese, R. (2015) Enhanced and Flexible Software Tools for X-ray Computed Tomography at the

478   Italian Synchrotron Radiation Facility Elettra. Fundamenta Informaticae, 141, 233-243.

479   Brown, M.A., Brown, M., Carlson, W.D., and Denison, D. (1999) Topology of syntectonic melt-

480   flow networks in the deep crust: Inferences from three- dimensional images of leucosome geometry

481   in migmatites. American Mineralogist, 84, 1793–1818.

482   Buffière, J-Y., Maire, E., Cloetens, P., Lormand, G., and Fougères, R. (1999) Characterization of

483   internal damage in a MMCp using X-ray synchrotron phase contrast microtomography. Acta

484   Materials, 47, 1613-1625.

485   Burvall, A., Lundstrom, U., Takman, P.A.C., Larsson, D.H., and Hertz H.M. (2011) Phase

486   retrieval in X-ray phase-contrast imaging suitable for tomography. Optics Express, 19, 10359.

487   Carlson, W.D. (2002) Scales of disequilibrium and rates of equilibration during metamorphism.

488   American Mineralogist, 87, 185–204.

489   Carlson, W.D. (2006) Three-dimensional imaging of earth and planetary materials. Earth and

490   Planetary Science Letters, 249, 133–147.

491   Carlson, W.D., and Denison, C. (1992) Mechanisms of porphyroblast crystallization: results

492   from high-resolution computed X-ray tomography. Science, 257, 1236-1239.

493   Carlson, W.D., Denison, C., and Ketcham, R.A. (1995) Controls on the nucleation and growth of

494   porphyroblasts: kinetics from natural textures and numerical models. Geological Journal, 30, 207-

495   225.

496   Chen, R.C., Dreossi, D., Mancini, L., Menk, R., Rigon, L., Xiao, T.Q., and Longo, R. (2012)

497   PITRE: software for phase-sensitive X-ray image processing and tomography reconstruction.

498   Journal of synchrotron radiation, 19, 836-845.

499   Cilona, A., Faulkner, D.R., Tondi, E., Agosta, F., Mancini, L., Rustichelli, A., Baud, P., and

500   Vinciguerra S. (2014) The effects of rock heterogeneity on compaction localization in porous

501   carbonates. Journal of Structural Geology, 67, 75-93.

502   Cloetens, P., Barrett, R., Baruchel, J., Guigay, J.P., and Schlenker, M. (1996) Phase objects in

503   synchrotron radiation hard X-ray imaging. Journal of Physics D, 29, 133-146.

504   Cloetens, P., Ludwig, W., Baruchel, J., Van Dyck, D., Van Landuyt, J., Guigay, J.P., and

505   Schlenker, M. (1999) Holotomography: Quantitative phase tomography with micrometer resolution

506   using hard synchrotron radiation X rays. Applied Physics Letters, 75, 2912-2914.

507   Cloetens, P., Pateyron-Salome, M., Buffiere, J.Y., Peix, G., Baruchel, J., Peyrin, F., and

508   Schlenker, M. (1997) Observation of microstructure and damage in materials by phase sensitive

509   radiography and tomography. Journal of Applied Physics, 81, 5878–5886.

510   Cnudde, V., and Boone, M.N. (2013) High-resolution X-ray computed tomography in

511   geosciences: A review of the current technology and applications. Earth-Science Reviews, 123, 1-

512   17.

513   Degruyter, W., Bachmann, O., and Burgisser A. (2010a) Controls on magma permeability in the

514   volcanic conduit during the climactic phase of the Kos Plateau Tuff eruption (Aegean Arc). Bulletin

515   of Volcanology, 72, 63–74.

516   Degruyter, W., Burgisser, A., Bachmann, O., and Malaspinas, O. (2010b) Synchrotron X-ray

517   microtomography and lattice Boltzmann simulations of gas flow through volcanic pumices.

518   Geosphere, 6, 470–481.

21

519   Denison, C., and Carlson, W.D. (1997) Three-dimensional quantitative textural analysis of

520   metamorphic rocks using high-resolution computed X-ray tomography: Part II. Application to

521   natural samples. Journal Metamorphic Geology, 15, 45–57.

522   Dowd, B.A., Campbell, G.H., Marr, R.B., Nagarkar, V., Tipnis, S., Axe, L., and Siddons, D.P.

523   (1999) Developments in synchrotron x-ray computed microtomography at the National Synchrotron

524   Light Source. Proceedings of SPIE 3772, Developments in X-Ray Tomography II, 224.

525   Ebel, D.S., Weisberg, M.K., Hertz, J., and Campbell, A.J. (2008) Shape, metal abundance,

526   chemistry, and origin of chondrules in the Renazzo (CR) chondrite. Meteoritics and Planetary

527   Science, 43, 1725–1740.

528   Faessel, M., and Jeulin, D. (2010) Segmentation of 3D microtomographic images of granular

529   materials with the stochastic watershed. Journal of Microscopy, 239, 17-31.

530   Fitzgerald, R. (2000) Phase sensitive X-ray imaging. Physics Today, 53, 23.

531   Friedrich, J.M., Wignarajah, D.P., Chaudhary, S., Rivers, M.L., Nehru, C.E., and Ebel D.S.

532   (2008) Three-dimensional petrography of metal phases in equilibrated L chondrites - Effects of

533   shock loading and dynamic compaction. Earth and Planetary Science Letters, 275, 172–180.

534   Fusseis, F., Xiao, X., Schrank, C., and De Carlo, F. (2014) A brief guide to synchrotron

535   radiation-based microtomography in (structural) geology and rock mechanics. Journal of Structural

536   Geology, 65, 1-16.

537   Giachetti, T., Burgisser, A., Arbaret, L., Druitt, T. H., and Kelfoun, K. (2011) Quantitative

538   textural analysis of Vulcanian pyroclasts (Montserrat) using multi-scale X-ray computed

539   microtomography: comparison with results from 2D image analysis. Bulletin of volcanology, 73,

540   1295-1309.

541   Godel, B., Barnes, S.J., Barnes, S.-J., and Maier, W.D. (2010) Platinum ore in 3D: insights from

542   high-resolution X-ray computed tomography. Geology, 38, 1127–1130.

543   Godel, B., Gonzalez-Alvarez, I., Barnes, S.J., Barnes, S.-J., Parker, P., and Day, J. (2012)

544   Sulfides and sulfarsenides from the Rosie Nickel Prospect, Duketon Greenstone Belt, Western

545   Australia. Economic Geology, 107, 275–294.

546   Godel, B., Barnes, S.J., Gürer, D., Austin, P., and Fiorentini, M.L. (2013) Chromite in

547   komatiites: 3D morphologies with implications for crystallization mechanisms. Contribution to

548   Mineralogy and Petrology, 165, 173–189.

549   Godel, B., Rudashevsky, N.S., Nielsen, T.F.D., Barnes, S.J., and Rudashevsky, V.N. (2014) New

550   constraints on the origin of the Skaergaard intrusion Cu–Pd–Au mineralization: Insights from high-

551   resolution X-ray computed tomography. Lithos, 190–191, 27–36.

552   Gualda, G.A.R. (2006), Crystal size distributions derived from 3D datasets: sample size versus

553   uncertainties. Journal of Petrology, 47, 1245–1254.

554   Gualda, G.A.R., and Rivers, M. (2006) Quantitative 3D petrography using X-ray tomography:

555   application to Bishop Tuff pumice clasts. Journal of Volcanology and Geothermal Research, 154,

556   48–62.

557   Gualda, G., Pamukcu, A., Claiborne, L., and Rivers, M. (2010) Quantitative 3D petrography

558   using X-ray tomography 3: documenting accessory phases with differential absorption tomography.

559   Geosphere, 6, 782–792.

560   Guigay, J.P., Langer, M., Boistel, R., and Cloetens, P. (2007) Mixed transfer function and

561   transport of intensity approach for phase retrieval in the Fresnel region. Optics Letters, 32, 1617–

562   1619.

563   Gureyev, T.E., and Nugent, K.A. (1996) Phase retrieval with the transport-of-intensity equation.

564   II. Orthogonal series solution for nonuniform illumination. Journal of the Optical Society of

565   America A, 13, 1670-1682.

566   Gureyev, T.E., and Nugent, K.A. (1997) Rapid quantitative phase imaging using the transport of

567   intensity equation. Optics Communication, 133, 339–346.

568   Gureyev, T.E., Nesterets, Y., Paganin, D., Pogany, A., and Wilkins, S. (2006) Linear algorithms

569   for phase retrieval in the Fresnel region. 2. partially coherent illumination. Optics Communications,

570   259, 569–580.

571   Gureyev, T.E., Nesterets, Y.I., Stevenson, A.W., Miller, P.R., Pogany, A., and Wilkins, S.W.

572   (2008) Some simple rules for contrast, signal-to-noise and resolution in in-line x-ray phase-contrast

573   imaging. Optics Express, 16, 3223-3241.

574   Henke, B.L., Gullikson, E.M., and Davis, J.C. (1993) X-ray interactions: photoabsorption,

575   scattering, transmission, and reflection at E=50-30000 eV, Z=1-92. Atomic Data and Nuclear Data

576   Tables, 54, 181-342.

577   Herman, G.T. (1980) Image reconstruction from projections: the fundamentals of computerized

578   tomography. Academic Press, New York.

579   Hersum, T.G., and Marsh, B.D. (2007) Igneous textures: on the kinetics behind the words.

580   Elements, 3, 247–252.

581   Higgins, M.D. (2000) Measurement of crystal size distributions. American Mineralogist, 85,

582   1105–1116.

583   Higgins, M.D. (2002) A crystal size-distribution study of the Kiglapait layered mafic intrusion,

584   Labrador, Canada: evidence for textural coarsening. Contribution to Mineralogy and Petrology,

585   144, 314–330.

586   Higgins, M.D. (2006) Quantitative textural measurements in igneous and metamorphic

587   petrology. Cambridge University Press, Cambridge, UK.

588   Jerram, D.A., Mock, A., Davis, G.R., Field, M., and Brown, R.J. (2009) 3D crystal size

589   distributions: a case study on quantifying olivine populations in kimberlites. Lithos, 112, 223–235.

590   Ketcham, R.A. (2005) Three dimensional textural measurements using high resolution

591   X ray computed tomography. Journal of Structural Geology, 27, 1217–1228.

592   Ketcham, R.A., and Carlson, W.D. (2001). Acquisition, optimization and interpretation of X-ray

593   computed tomographic imagery: applications to the geosciences. Computers and Geosciences, 27,

594   381–400.

595   Ketcham, R.A., Meth, C., Hirsch, D.M., and Carlson, W.D. (2005) Improved methods for

596   quantitative analysis of three-dimensional porphyroblastic textures. Geosphere, 1, 42–59.

597   Langer, M., Boistel, R., Pagot, E., Cloetens, P., and Peyrin, F. (2010) X-ray in-line phase

598   microtomography for biomedical applications. Microscopy: Science, Technology, Applications and

599   Education.

600   Lev, A., Zucker, S.W., and Rosenfeld, A. (1977) Iterative Enhancemnent of Noisy Images.

601   Systems, Man and Cybernetics, IEEE Transactions, 7, 435-442.

602   Lin, Q., Neethling, S. J., Dobson, K. J., Courtois, L., and Lee, P. D. (2015) Quantifying and

603   minimising systematic and random errors in X-ray micro-tomography based volume measurements.

604   Computers and Geosciences, 77, 1-7.

605   Madonna, C., Quintal, B., Frehner, M., Almqvist, B.S.G., Tisato, N., Pistone, M., Marone, F.,

606   and Saenger, E.H. (2013) Synchrotron-based X-ray tomographic microscopy for rock physics

607   investigations. Geophysics, 78, D53-D64.

608   Maire E. and Withers P.J. (2014) Quantitative X-ray tomography. International Materials

609   Reviews; 59, 1-43.

610   Mancini, L., Reiner, E., Cloetens, P., Gastaldi, J., Härtwig, J., Schlenker, M., and Baruchel J.

611   (1998) Investigation of defects in AlPdMn icosahedral quasicrystals by combined synchrotron X-

612   ray topography and phase radiography. Philosophical Magazine A, 78, 1175–1194.

613   Marinoni, N., Voltolini, M., Mancini, L., Vignola, P., Pagani, A., and Pavese, A., (2009) An

614   investigation of mortars affected by alkali-silica reaction by X-ray synchrotron microtomography: a

615   preliminary study. Journal of Materials Science, 44 – 21.

616   Marsh, B.D. (1988) Crystal size distribution (CSD) in rocks and the kinetics and dynamics of

617   crystallization. 1. Theory. Contribution to Mineralogy and Petrology, 99, 277–291.

618   Marsh, B.D. (1998) On the interpretation of crystal size distributions in magmatic systems,

619   Journal of Petrology, 39, 553–599.

620   Marsh, B.D. (2007) Crystallization of silicate magmas deciphered using crystal size

621   distributions. Journal of the American Ceramic Society, 90, 746–757.

622   Mayo, S.C., Stevenson, A.W., and Wilkins, S.W. (2012) In-line phase-contrast X-ray imaging

623   and tomography for materials science. Materials, 5, 937-965.

624   Mohammadi, S., Larsson, E., Alves, F., Dal Monego, S., Biffi, S., Garrovo, C., Lorenzon, A.,

625   Tromba, G., and Dullin, C. (2014) Quantitative evaluation of a single-distance phase-retrieval

626   method applied on in-line phase-contrast images of a mouse lung. Journal of synchrotron radiation,

627   21, 784-789.

628   Münch, B., Trtik, P., Marone, F., and Stampanoni, M. (2009) Stripe and ring artifact removal

629   with combined wavelet-Fourier filtering. Optics Express 17, 8567–8591.

630   Paganin, D., and Nugent, K.A. (1998) Noninterferometric phase imaging with partially coherent

631   light. Physical Review Letters, 80, 2586–2589.

632   Paganin, D., Mayo, S.C., Gureyev, T.E., Miller, P.R., and Wilkins, S.W. (2002) Simultaneous

633   phase and amplitude extraction from a single defocused image of a homogeneous object. Journal of

634   Microscopy, 206, 33-40.

635   Pal, N.R, and Pal S.K. (1993) A review on image segmentation techniques. Pattern Recognition,

636   26: 1277–1294.

637   Pamukcu, A.S., and Gualda G.A.R. (2010) Quantitative 3D petrography using X-ray tomography

638   2: combining information at various resolutions. Geosphere, 6, 775–781.

639   Pamukcu, A.S., Gualda, G.A.R., and Anderson, A.T. (2012) Crystallization stages of the Bishop

640   Tuff magma body recorded in crystal textures in pumice clasts. Journal of Petrology, 63, 589–609.

26

641   Pfeiffer, F., Weitkamp, T., Bunk, O., and David, C. (2006) Phase retrieval and differential phase-

642   contrast imaging with low-brilliance x-ray sources. Nature Physics, 2, 258–61.

643   Polacci, M., Baker, D.R., Mancini, L., Tromba, G., and Zanini, F. (2006) Three-dimensional

644   investigation of volcanic textures by X-ray microtomography and implications for conduit

645   processes. Geophysical Research Letters, 33, L13312.

646   Polacci, M., Baker, D.R., Mancini, L., Favretto, S., and Hill, R.J. (2009) Vesiculation in magmas

647   from Stromboli and implications for normal Strombolian activity and paroxysmal explosions in

648   basaltic systems. Journal of Geophysical Research, 114, B01206.

649   Polacci, M., Baker, D.R, LaRue, A., Mancini, L., and Allard, P. (2012) Degassing behaviour of

650   vesiculated basaltic magmas: an example from Ambrym volcano, Vanuatu Arc. Journal of

651   Volcanology and Geothermal Research, 233-234, 55-64.

652   Ralph, J., and Chau, I. (2014) Mindat.org.

653   Rivers, M. (1998). Tutorial introduction to X-ray computed microtomography data processing.

654   University of Chicago.

655   Sayab, M., Suuronen, J.-P., Hölttä, P., Aerden, D., Lahtinen, R., and Petteri Kallonen, A. (2014)

656   High-resolution X-ray computed microtomography: A holistic approach to metamorphic fabric

657   analyses. Geology, 43, 55–58.

658   Schneider, C.A., Rasband, W.S., and Eliceiri, K.W. (2012) NIH Image to ImageJ: 25 years of

659   image analysis. Nature Methods, 9, 671–675.

660   Sijbers, J., and Postnov, A. (2004) Reduction of ring artefacts in high resolution micro-CT

661   reconstructions. Physics in Medicine and Biology, 49, N247–N253.

662   Smith, T.M., Tafforeau, P., Reid, D. J., Pouech, J., Lazzari, V., Zermeno, J.P., Guatelli-Steinberg

663   D., Olejniczakb, A.J., Hoffmang, A., Radovčićh, J., Makaremii, M., Toussaintj, M., Stringer C., and

664   Hublin, J.J. (2010). Dental evidence for ontogenetic differences between modern humans and

665   Neanderthals. Proceedings of the National Academy of Sciences, 107, 20923-20928.

666   Snigirev, A., Snigireva, I., Kohn, V., Kuznetsov, S., and Schelokov, I. (1995) On the possibilities

667   of X-ray phase contrast imaging by coherent high energy synchrotron radiation. Review of

668   Scientific Instruments, 66, 5486–5492.

669   Tafforeau, P., Boistel, R., Boller, E., Bravin, A., Brunet, M., Chaimanee, Y., Cloetens, P., Feist,

670   M., Hoszowska, J., Jaeger, J.-J., Kay, R. F., Lazzari, V., Marivaux, L., Nel, A., Nemoz, C.,

671   Thibault, X., Vignaud, P., and Zabler, S. (2006) Applications of X-ray synchrotron

672   microtomography for non-destructive 3D studies of paleontological specimens. Applied Physics A,

673   83, 195-202.

674   Teague, M.R. (1983) Deterministic phase retrieval: a Green's function solution, Journal of the

675   Optical Society of America, 73, 1434–1441.

676   Titarenko, V., Titarenko, S., Withers, P. J., De Carlo, F., and Xiao, X. (2010) Improved

677   tomographic reconstructions using adaptive time-dependent intensity normalization. Journal of

678   Synchrotron Radiation 17, 689–699.

679   Tromba, G., Longo, R., Abrami, A., Arfelli, F., Astolfo, A., Bregant, P., Brun, F., Casarin, K.,

680   Chenda, V., Dreossi, D., Hola, M., Kaiser, J., Mancini, L., Menk, R.H., Quai, E., Quaia, E., Rigon,

681   L., Rokvic, T., Sodini, N., Sanabor, D., Schultke, E., Tonutti, M., Vascotto, A., Zanconati, F., Cova,

682   M., and Castelli, E. (2010) The SYRMEP Beamline of Elettra: Clinical Mammography and Bio-

683   medical Applications. AIP Conference Proceedings, 1266, 18-23.

684   Tsuchiyama, A., Hanamoto, T., Nakashima, Y., and Nakano, T. (2000) Quantitative evaluation

685   of attenuation contrast of minerals by using a medical X-ray CT scanner. Journal of Mineralogical

686   and Petrological Sciences, 95, 125-137.

687   Tsuchiyama, A., Uesugi, K., Nakano, T., and Ikeda, S. (2005) Quantitative evaluation of

688   attenuation contrast of X-ray computed tomography images using monochromatized beams.

689   American Mineralogist, 90, 132–142.

690   Tsuchiyama, A., Uesugi, M., Matsushima, T., Michikami, T., Kadono, T., Nakamura, T., Uesugi,

691   K., Nakano, T., Sandford, S.A., Noguchi, R., Matsumoto, T., Matsuno, J., Nagano, T., Imai, Y.,

692   Takeuchi, A., Suzuki, Y., Ogami, T., Katagiri, J., Ebihara, M., Ireland, T.R., Kitajima, F., Nagao,

693   K., Naraoka, H., Noguchi, T., Okazaki, R., Yurimoto, H., Zolensky, M.E., Mukai, T., Abe, M.,

694   Yada, T., Fujimura, A., Yoshikawa, M., and Kawaguchi, J. (2011) Three-dimensional structure of

695   Hayabusa samples: origin and evolution of Itokawa Regolith. Science, 333, 1125–1128.

696   Tsuchiyama, A., Nakano, T., Uesugi, K., Uesugi, M., Takeuchi, A., Suzuki, Y., Noguchi, R.,

697   Matsumoto, T., Matsuno, J., Nagano, T., Imai, Y., Nakamura, T., Ogami, T., Noguchi, T., Abe, M.,

698   Yada, T., and Fujimura, A. (2013) Analytical dual- energy microtomography: A new method for

699   obtaining three-dimensional phase images and its application to Hayabusa samples. Geochimica et

700   Cosmochimica Acta, 116, 5–16.

701   Uesugi, K., Tsuchiyama, A., Nakano, T., Suzuki, Y., Yagi, N., Umetani, K., and Kohmura, Y.

702   (1999) Development of microtomography imaging system for rock and mineral samples.

703   Proceedings SPIE 3772, Developments in X-Ray Tomography II, 214.

704   Uesugi, M., Uesugi, K., and Oka, M. (2010) Non-destructive observation of meteorite chips

705   using quantitative analysis of optimized X-ray micro-computed tomography. Earth and Planetary

706   Science Letters, 299, 359–367.

707   Uesugi, M., Uesugi, K., Takeuchi, A., Suzuki, Y., Hoshino, M., and Tsuchiyama, A. (2013)

708   Three-dimensional observation of carbonaceous chondrites by Synchrotron radiation X-ray CT -

709   quantitative analysis and developments for the future sample return missions. Geochimica et

710   Cosmochimica Acta., 116, 17–32.

711   Van Nieuwenhove, V., De Beenhouwer, J., De Carlo, F., Mancini, L., Marone, F., Sijbers, J.,

712   (2015) Dynamic intensity normalization using eigen flat fields in X-ray imaging, Optics Express,

713   23-21, 27975-27989.

714   Voltolini, M., Zandomeneghi, D., Mancini, L., and Polacci, M. (2011) Texture analysis of

715   volcanic rock samples: quantitative study of crystals and vesicles shape preferred orientation from

716   X-ray microtomography data. Journal of Volcanology and Geothermal Research, 202, 83-95.

717   Weitkamp, T., Haas, D., Wegrzynek, D., and Rack, A. (2011) ANKAphase: software for single-

718   distance phase retrieval from inline X-ray phase-contrast radiographs. Journal of Synchrotron

719   Radiation, 18, 617–629.

720   Zandomeneghi, D., Voltolini, M., Mancini, L., Brun, F., Dreossi, D., and Polacci, M. (2010)

721   Quantitative analysis of X-ray microtomography images of geomaterials: Application to volcanic

722   rock. Geosphere, 6, 793-804.

723   Zanolli, C., Bondioli, L., Coppa, A., Dean, C.M., Bayle, P., Candilio, F., Capuani, S., Dreossi,

724   D., Fiore, I., Frayer, D.W., Libsekal, Y., Mancini, L., Rook, L., Medin Tekle, T., Tuniz, C., and

725   Macchiarelli, R. (2014) The late Early Pleistocene human dental remains from Uadi Aalad and

726   Mulhuli-Amo (Buia), Eritrean Danakil: Macromorphology and microstructure. Journal of Human

727   Evolution, 74, 96–113.

728   Zucali, M., Voltolini, M., Ouladdiaf, B., Mancini, L., and Chateigner, D. (2014a) The 3D

729   quantitative lattice and shape preferred orientation of a mylonitised metagranite from Monte Rosa

730   (Western Alps): combining neutron diffraction texture analysis and synchrotron X-ray

731   microtomography. Journal of Structural Geology, 63, 91–105.

732   Zucali, M., Barberini, V., Voltolini, M., Ouladdiaf, B., Chateigner, D., and Mancini, L. (2014b)

733   Quantitative 3D microstructural analysis of naturally deformed amphibolite from the Southern Alps

734   (Italy): Microstructures, LPO, and seismic anisotropy from a fossil extensional margin, in Rock

735   Deformation From Field, Experiments and Theory: A Volume in Honour of Ernie Rutter.

736   Geological Society Special Publication, 409, 201-222.

737

738   **Figure captions**

30

739   Figure 1. Comparison of 2D and 3D textural analysis approaches.

740   Figure 2. Plot showing the linear attenuation coefficient (μ) of basaltic and trachytic glasses and

741   anorthite, albite, labradorite and sanidine crystals as a function of Energy (keV). Linear attenuation

742   coefficients (μ) of each phase were obtained from the National Institute of Standards and

743   Technology (NIST) database (http://physics.nist.gov/PhysRefData/FFast/html/form.html).

744   Figure 3. (a) Reconstructed axial slice of Stromboli pumice before phase-retrieval processing. (b)

745   Thresholded binary image, illustrating segmentation of plagioclase crystals from basaltic glass and

746   vesicles.

747   Figure 4. Reconstructed axial slice of the synthetic trachyte samples before (a) and after (b)

748   phase-retrieval processing. The image in (b) shows alkali feldspar (light gray), trachytic glass (dark

749   gray), vesicles (black), clinopyroxenes and oxides (white).

750   Figure 5. Scheme of the proposed phase-retrieval procedure. # Commercial software; * open-

751   source software.

752   Figure 6. Plot of $\gamma = \delta/\beta$ for basaltic and trachytic glasses and labradorite, anorthite, anorthoclase

753   and sanidine crystals as a function of Energy (keV). The refractive index was obtained using the

754   CXRO X-ray database (http://henke.lbl.gov/optical_constants/) (Henke et al., 1993).

755   Figure 7. Comparison of edge effects between phase-contrast and phase-retrieved images. (a)

756   Raw image obtained in phase-contrast mode for Stromboli basaltic pumice. (b) Result from the TIE

757   phase-retrieval algorithm with a δ-to-β ratio optimized for plagioclase of the Stromboli basaltic

758   pumice. (c) Raw image obtained in phase-contrast mode for the synthetic trachyte. (b) Result from

759   the TIE phase-retrieval algorithm with a δ-to-β ratio optimized for sanidine of the trachyte.

760   Figure 8. (a) Reconstructed axial slice of the Stromboli pumice after phase-retrieval processing.

761   (b) Thresholded image after phase-retrieval illustrating segmentation of plagioclases from basaltic

762   glass and vesicles. Note that noise is still present after segmentation. (c) Second segmentation

763   consisting in the approximate isolation of the shape of plagioclase, and in deleting background

31

764   noise as much as possible. (d) Mask of plagioclase crystals. (e) After (d), the AND operator in *Fiji*

765   was applied to combine both the first segmentation (b) and the mask (d) in order to segment

766   plagioclase crystals from basaltic glass and vesicles.

767   Figure 9. Scheme of the image processing protocol that has been used to segment plagioclase

768   from the background matrix in the Stromboli pumice.

769   Figure 10. Volume renderings of crystals. (a) Volume renderings of the segmented plagioclases

770   in Stromboli pumice sample; the maximum length of the largest crystal is ~ 1 mm. (b) Volume

771   rendering of the segmented alkali feldspars in the synthetic trachyte sample; the average length of

772   each lamella within spherulites is 150 μm.

2D vs 3D

Figure 1

Advantages and special features

- Image mapping of large area of the sample at high resolution (pixel size <1 µm).
- Phase abundance can be determined
- Lattice orientation of crystals is available
- Chemical compositions of major and trace elements can be determined

- Large volume of sample can be imaged
- Non-destructive 3D imaging and analysis
- Textural features of the sample can be visualized in 3D
- Volumetric analysis: phase abundance and size can be directly measured in 3D
- Preferred orientation and connectivity of objects can be measured in 3D
- Stereological conversion are not necessary
- Experimental apparatus are available to perform 4D experiments

Limitations

- Destructive procedures are needed to prepare thin sections
- Stereological conversion is needed
- Population of crystals are described statistically

- Not always possible to identify and separate easily different minerals, due to similar density contrast and crystal sizes smaller than spatial resolution
- Image processing and analysis are time consuming

Figure 2
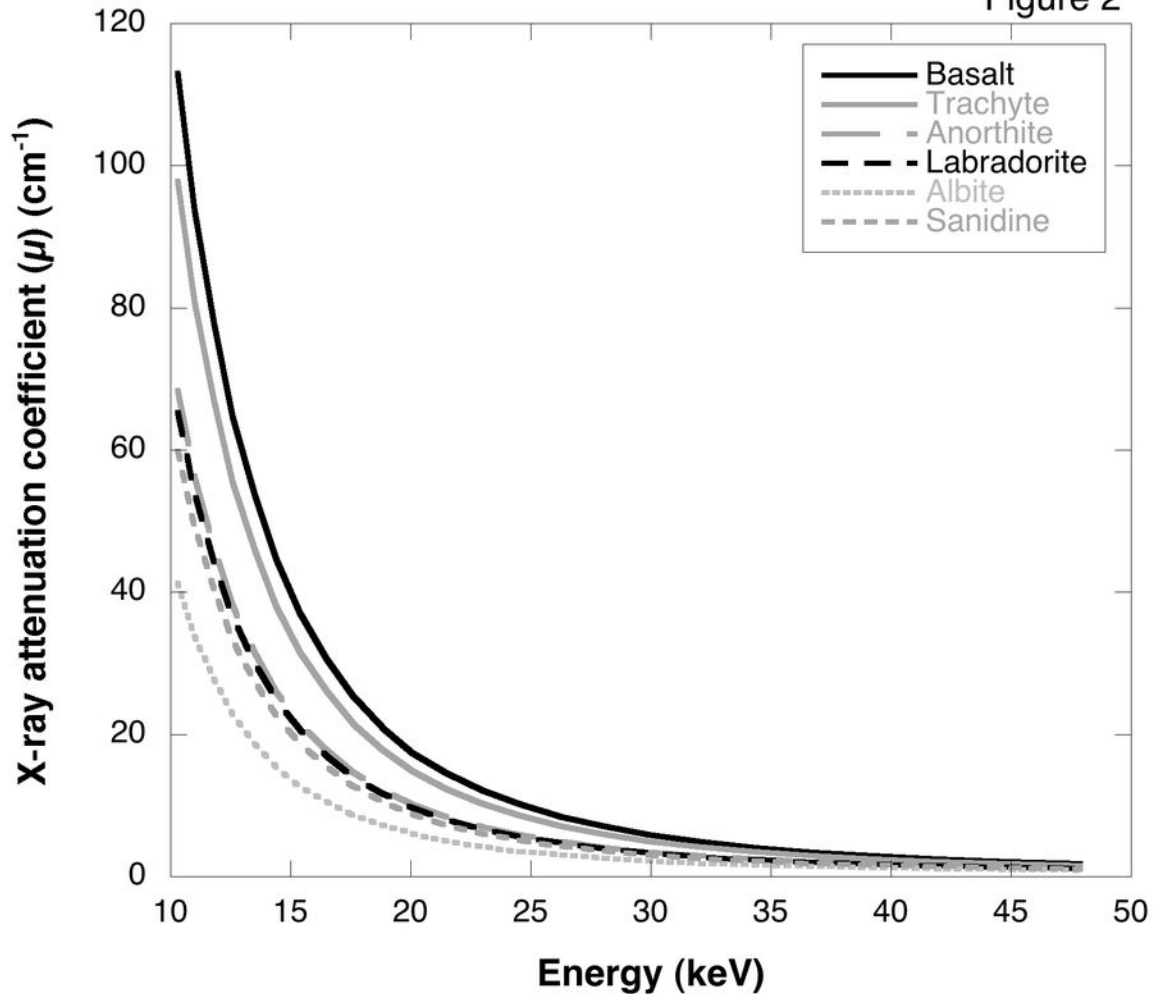
(a)

Figure 3a
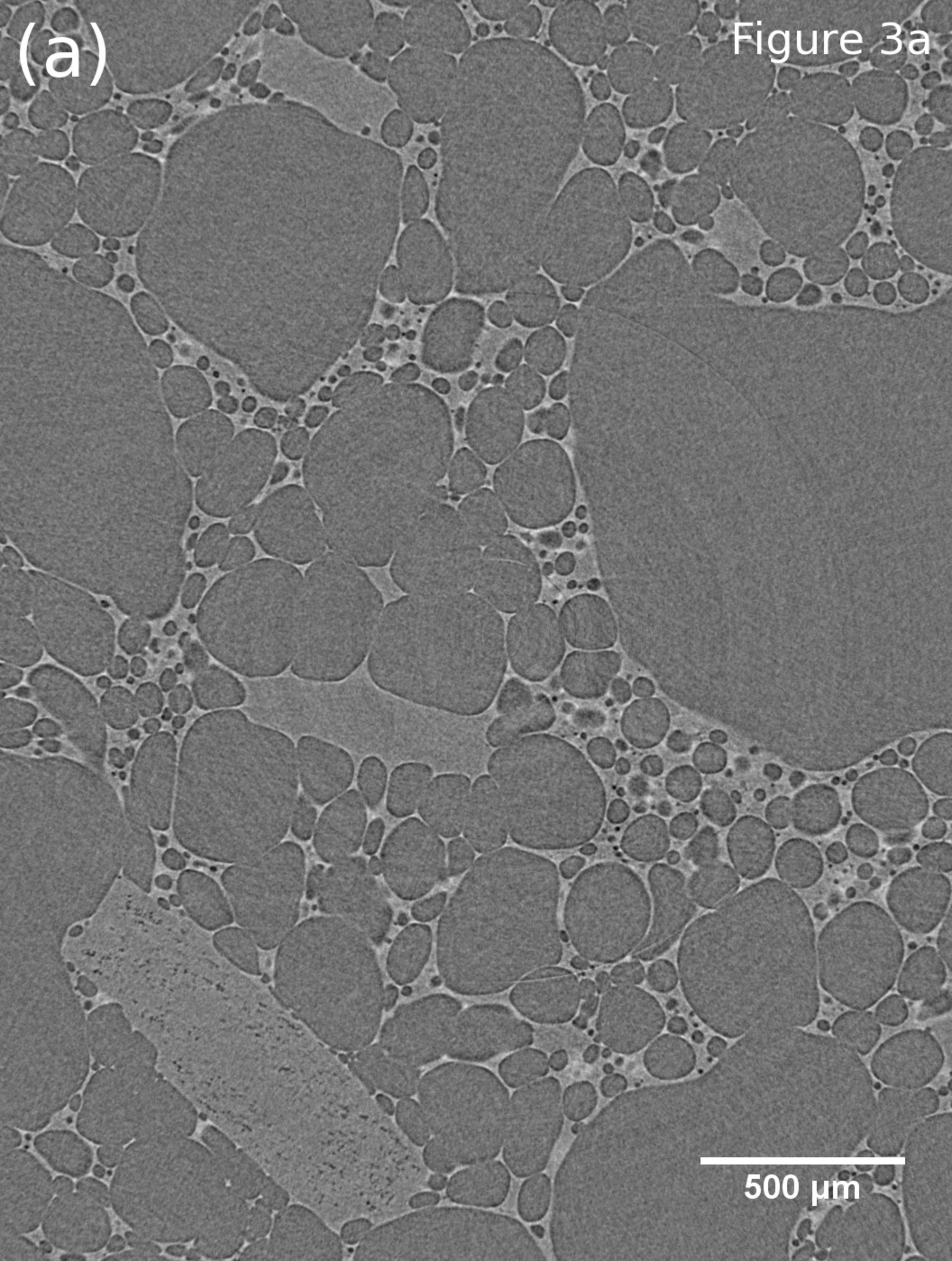
500 µm

(b)

Figure 3b

500 μm

(a)

Figure 4a

500 μm

(b)
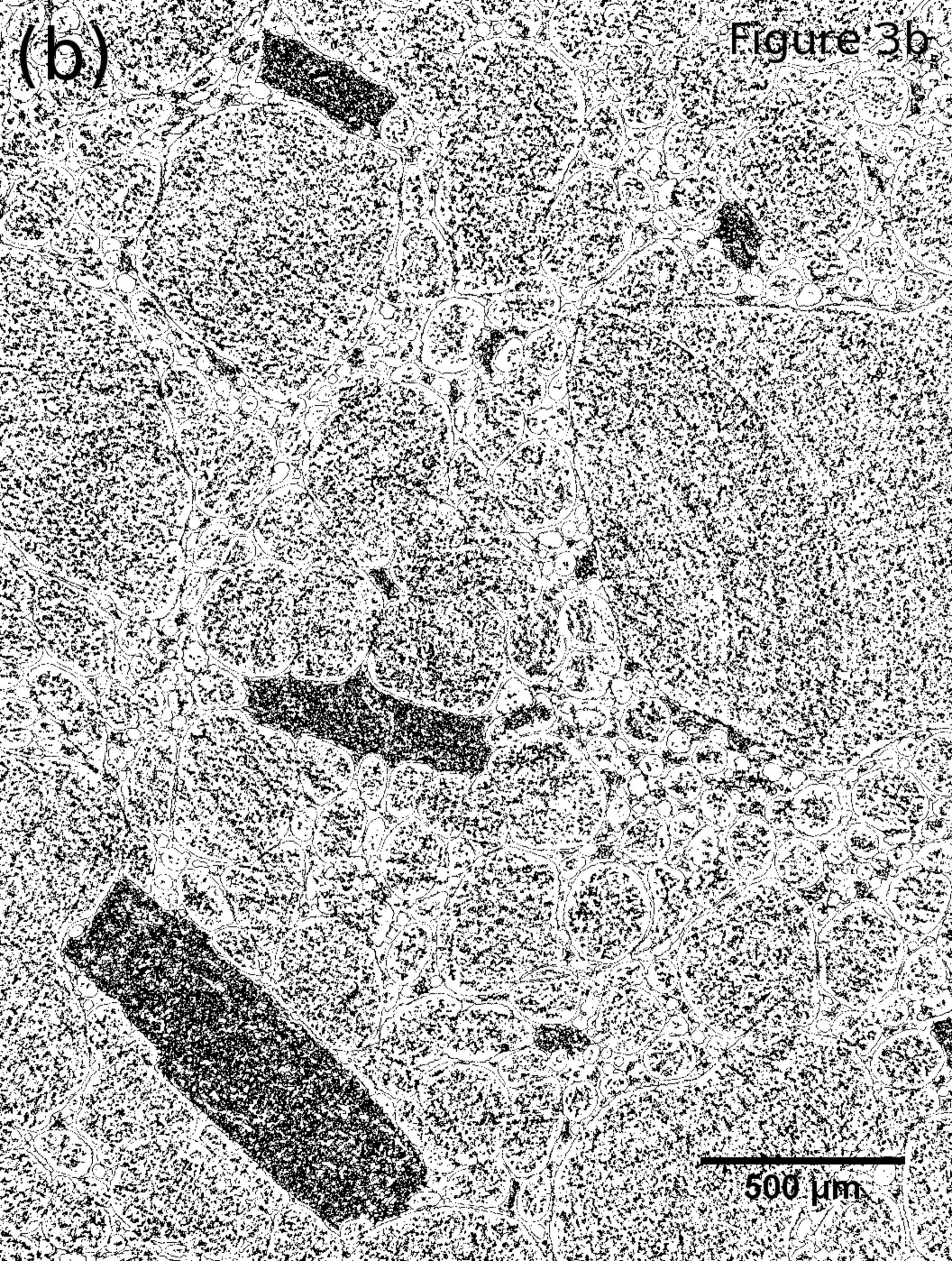
Figure 4b

500 μm
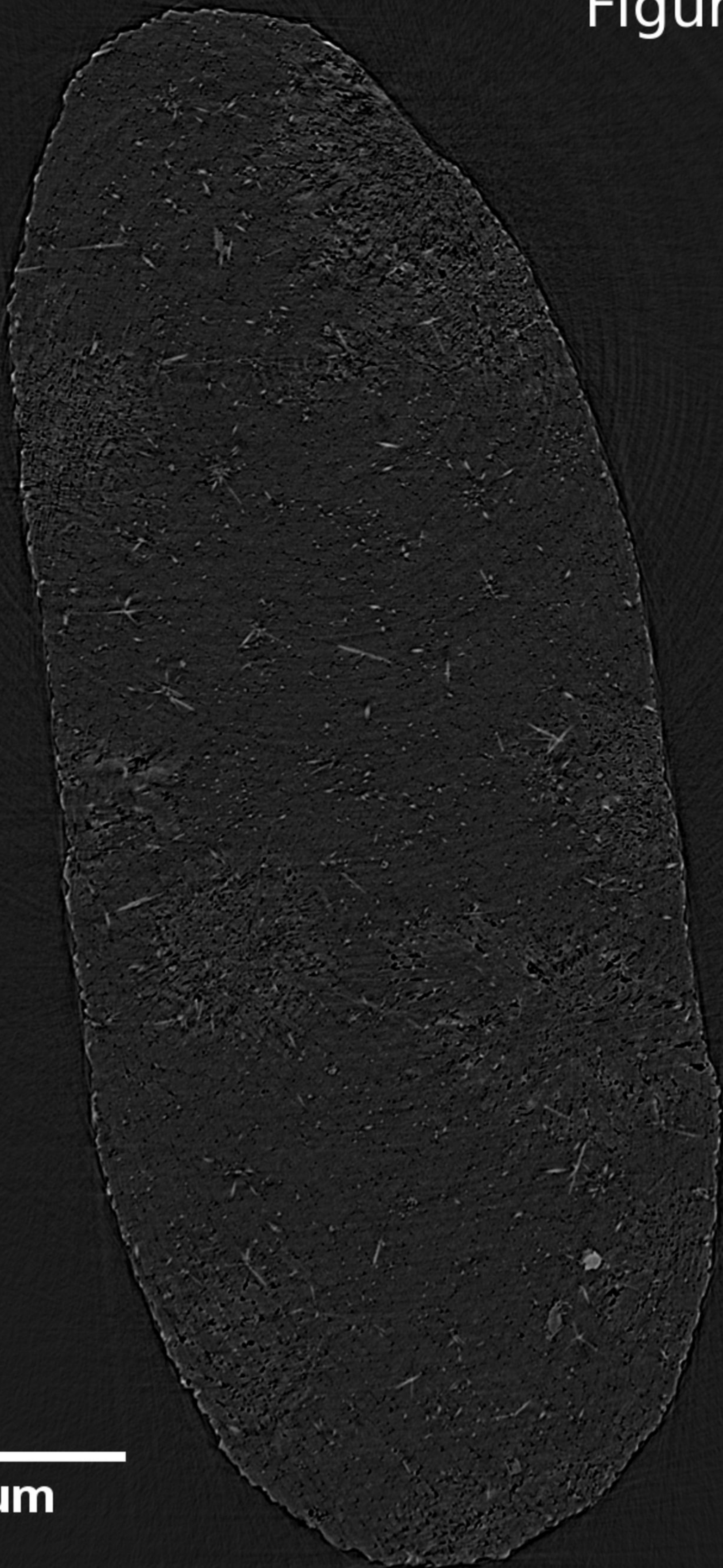
Figure 5
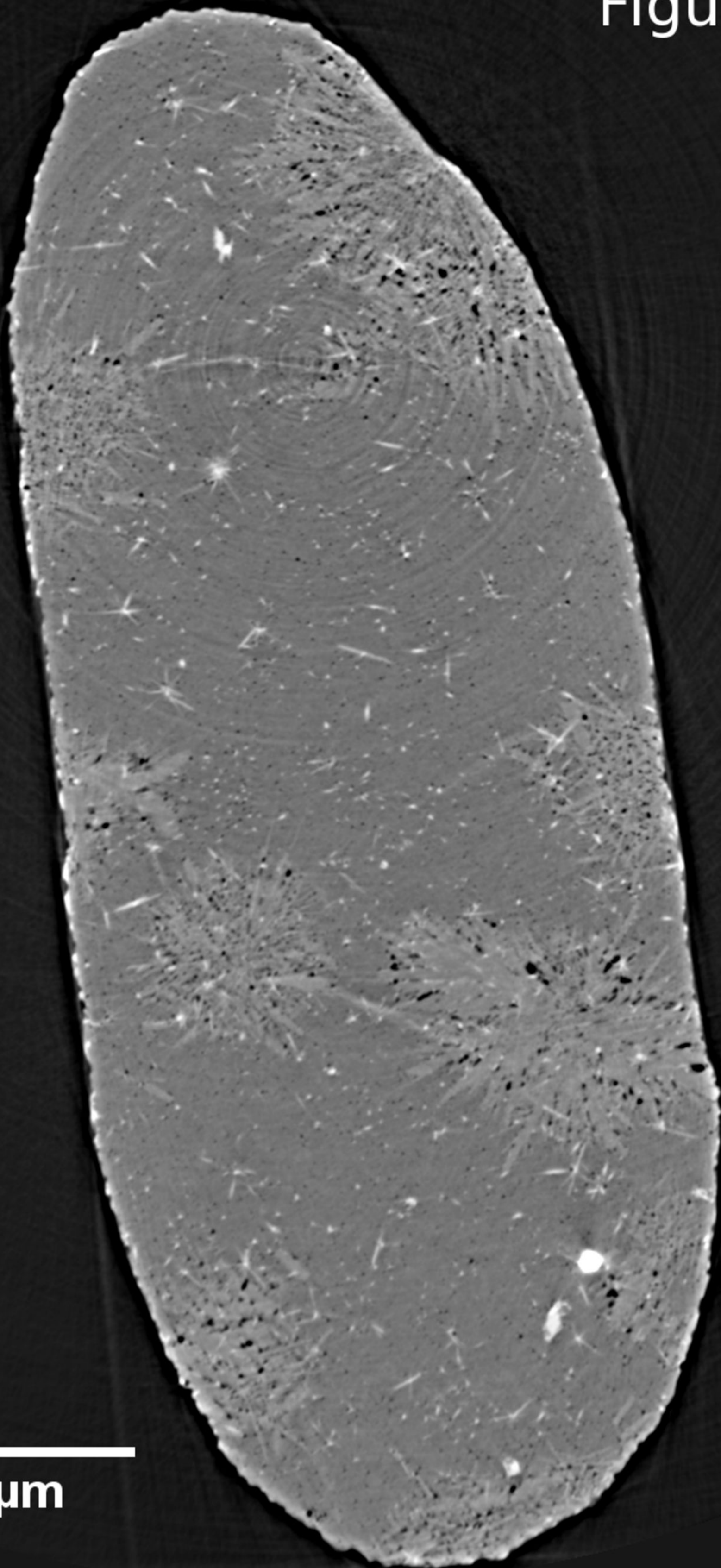
Pre-segmentation

- Phase-retrieval processing -

Calculation of Refractive Index

The calculation of the refractive index can be obtained using the CXRO X-ray database (Henke et al. 1993) (http://henke.lbl.gov/optical_constants/getdb2.html)

δ = refractive index decrement
β = absorption index

To obtain δ and β several parameters are needed:

- Chemical formula of the phase of interest
- Density (g/cm^3) of the phase of interest
- Photon energy (keV) used during the X-ray µCT acquisition

Single-distance phase-retrieval TIE algorithm

Available software

X-TRACT software (CSIRO group) [#]
ANKA phase software (Weitkamp et al. 2011) [*]
PITRE software (Pfeiffer et al. 2006) [*]
TomoPy software (Gürsoy et al. 2014) [*]
SYRMEP Tomo Project (Brun et al. 2015) [*]

X-TRACT software
(used in this study)

For slices reconstruction several parameters are requested:

Photon energy (KeV)

Sample-detector distance

$\delta/\beta = \gamma$

The calculated value of γ (Fig. 6) may be tuned to obtain:

- Cancellation of phase-contrast artifacts
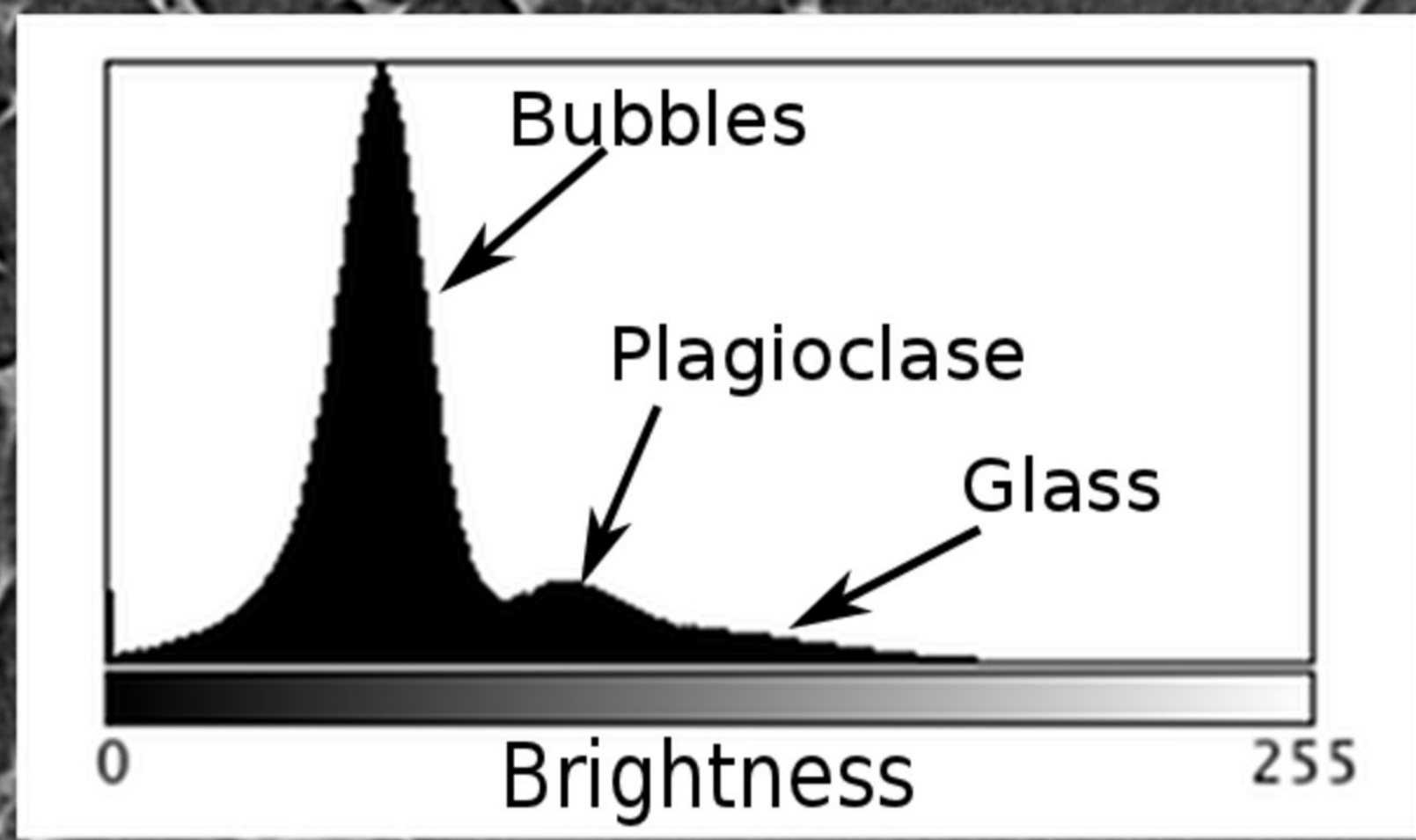- Better contrast between phases avoiding blurring

Figure 6

(a)

Lack of contrast

Brightness

0

255

500 μm

Figure 7a

(b)

Bubbles

Plagioclase

Glass

0   Brightness   255

500 µm

Figure 7b

(c)

Lack of contrast

Brightness

0   255

100 µm

Figure 7c

(d)

Glass

Sanidine

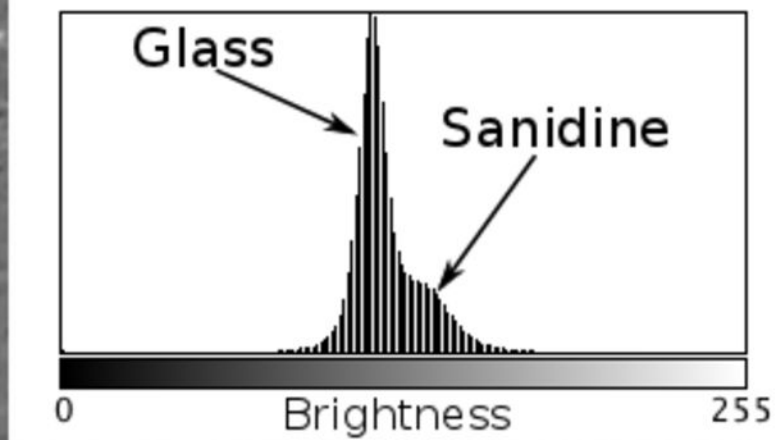0   Brightness   255

100 µm
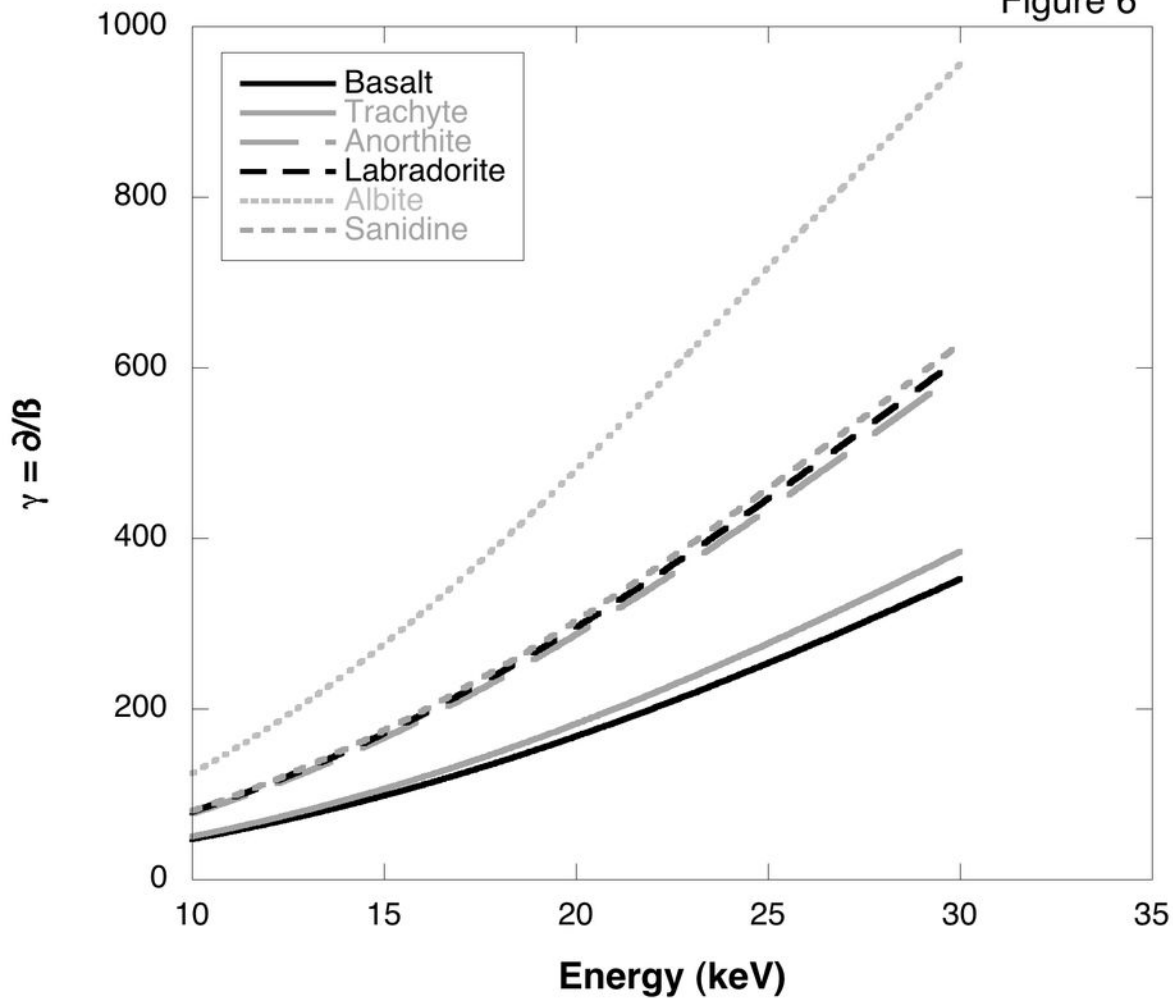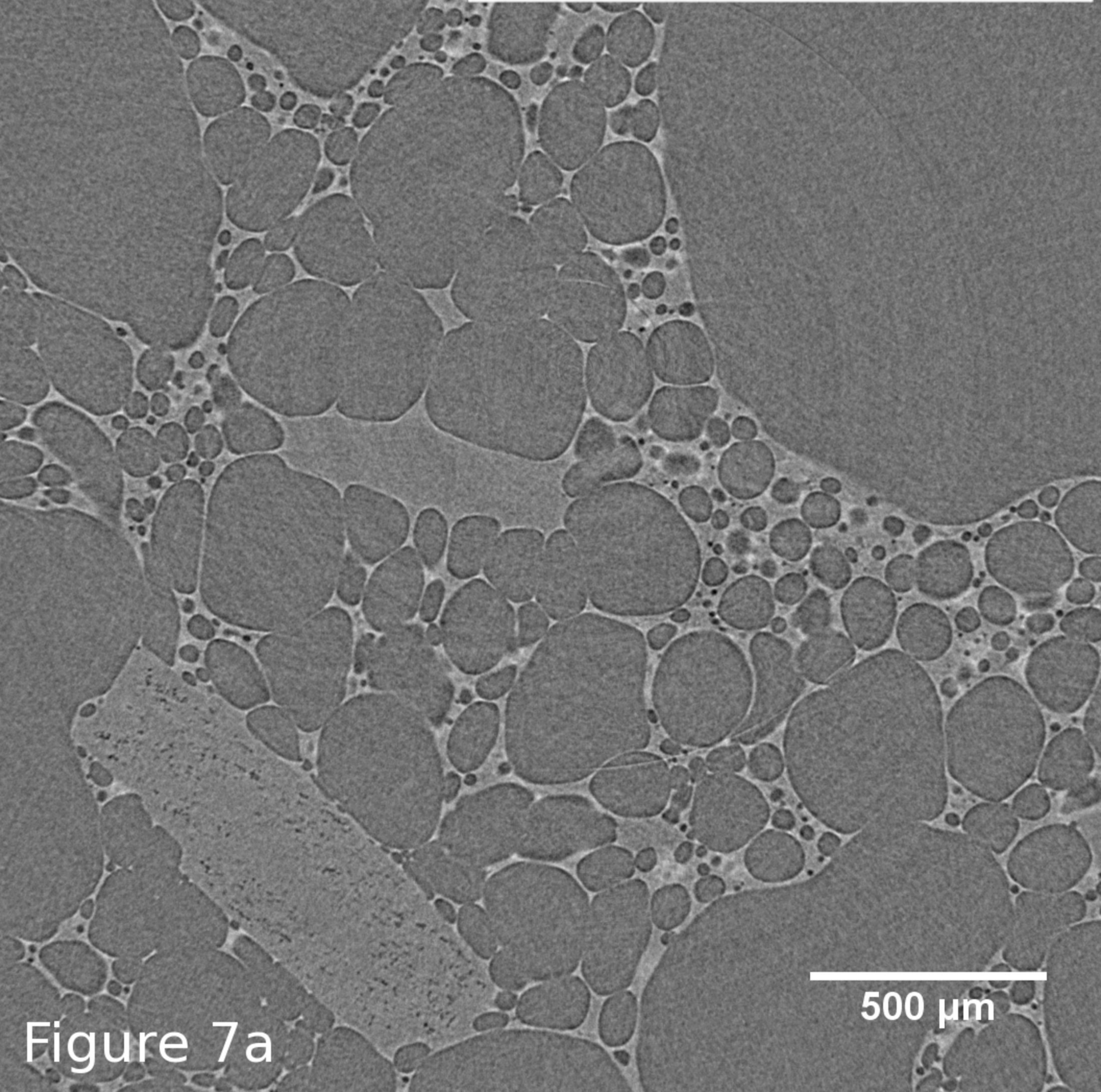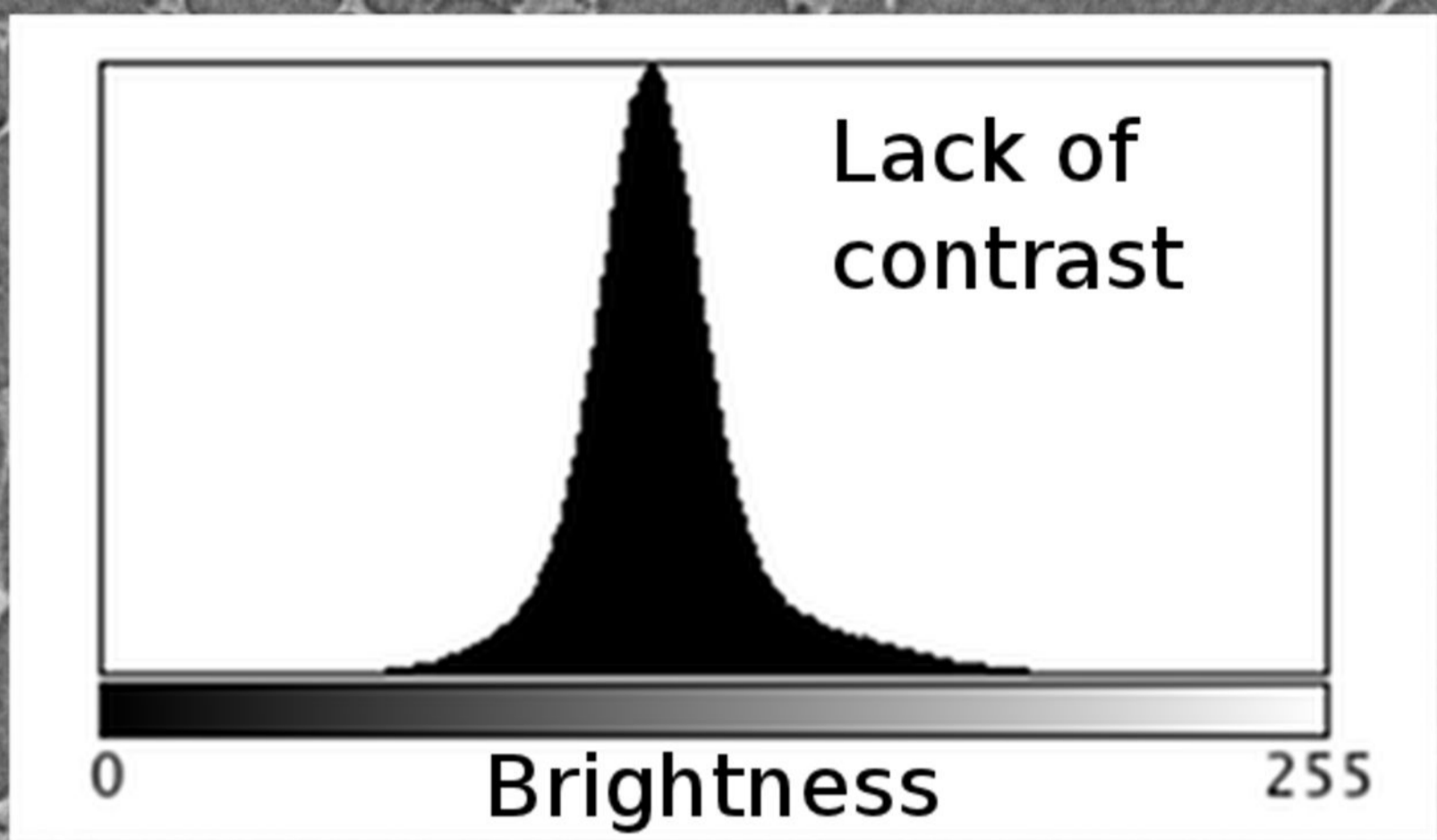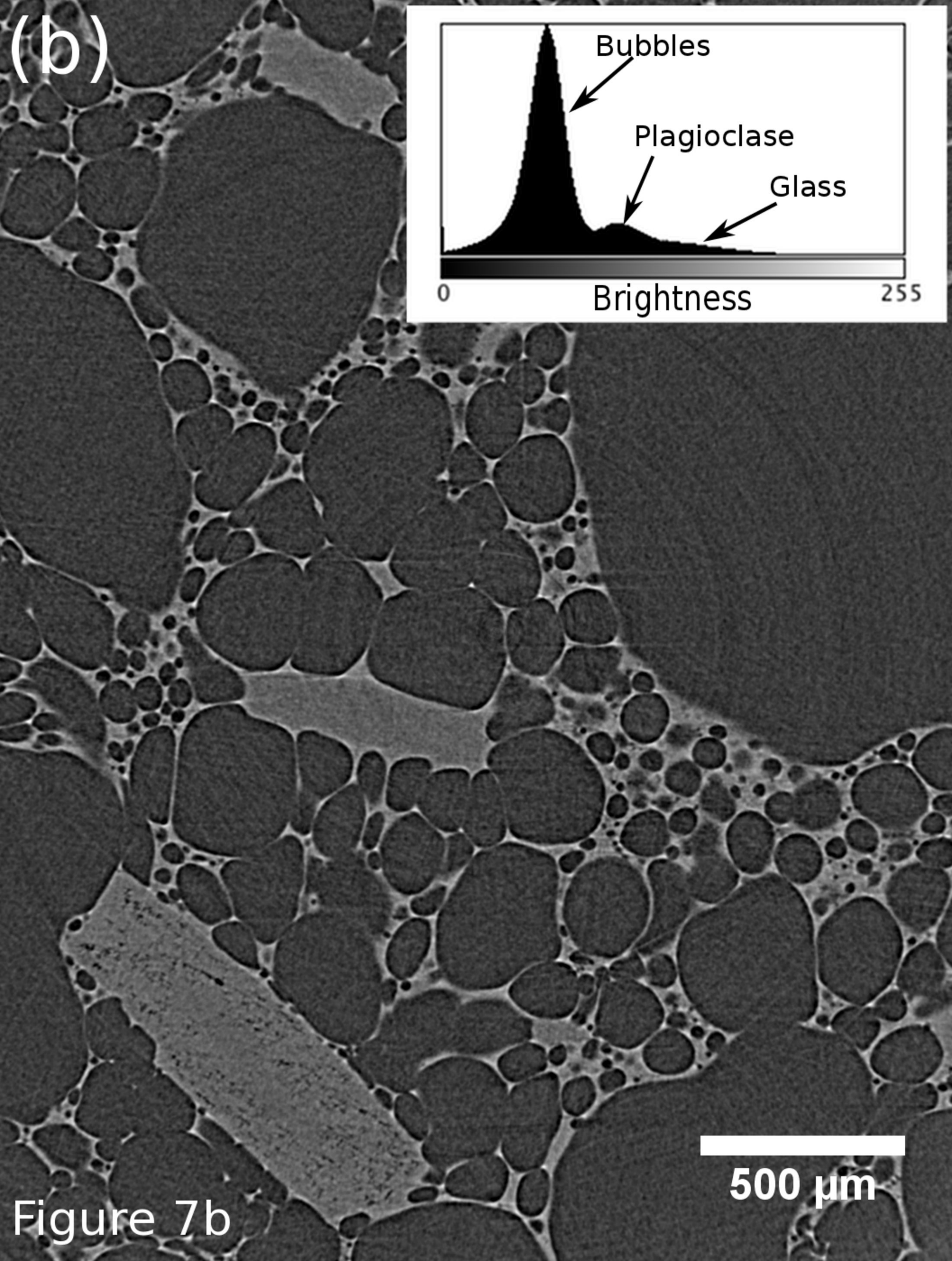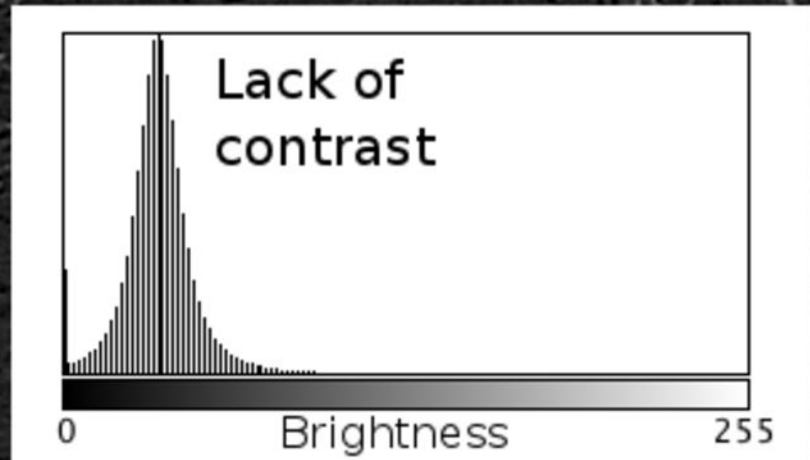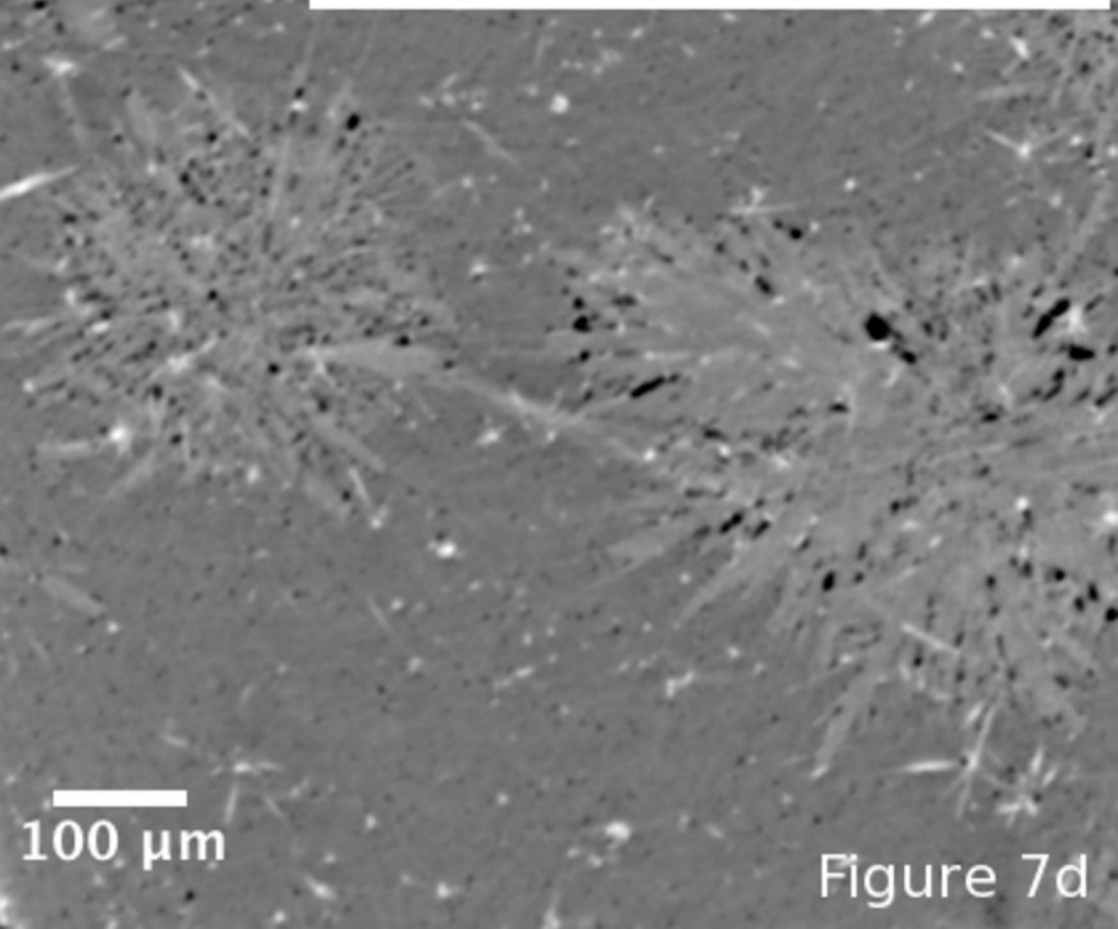
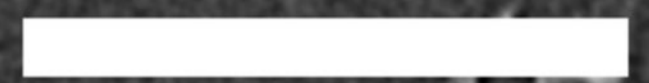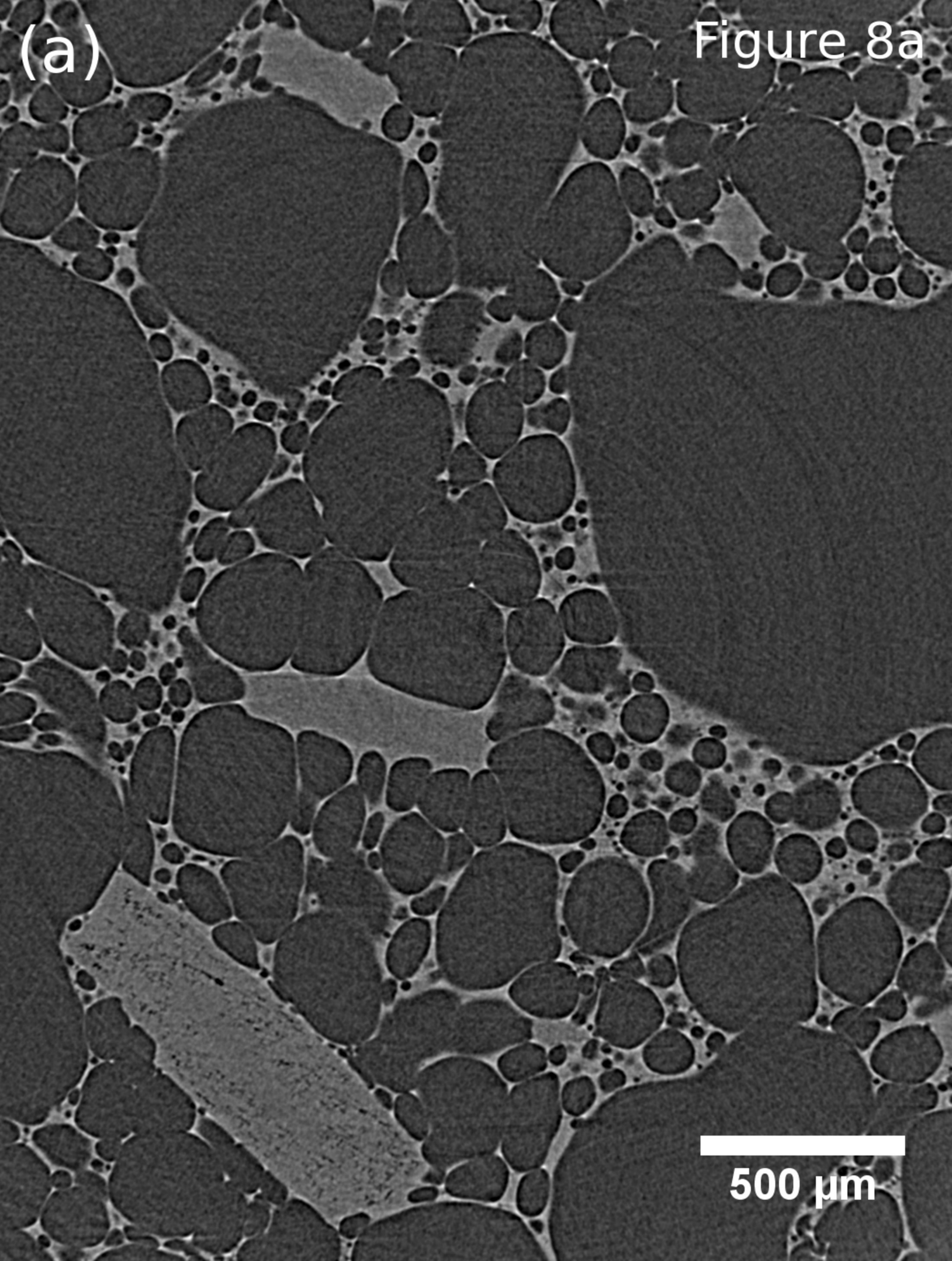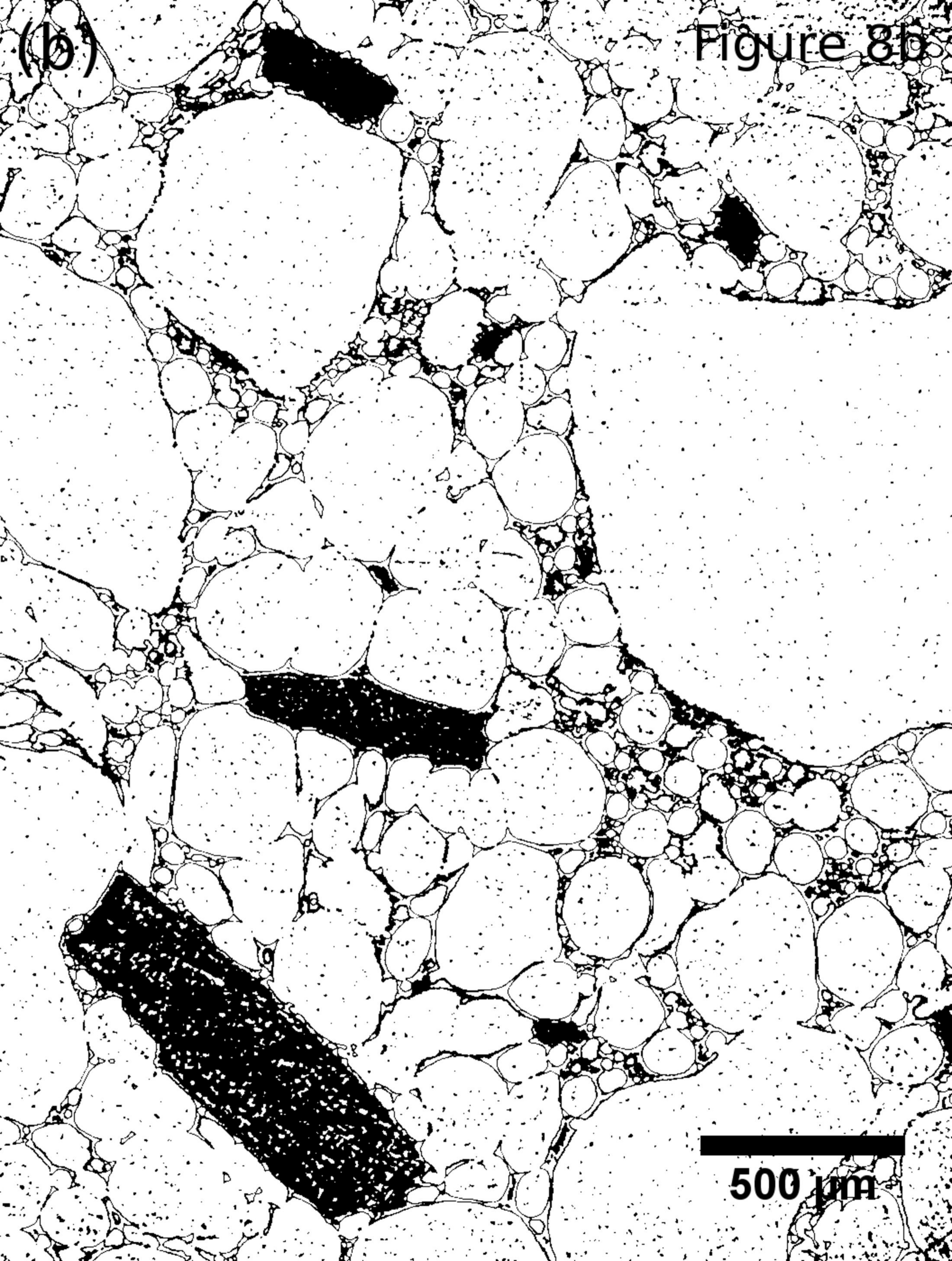Figure 7d

(a) Figure 8a

500 μm

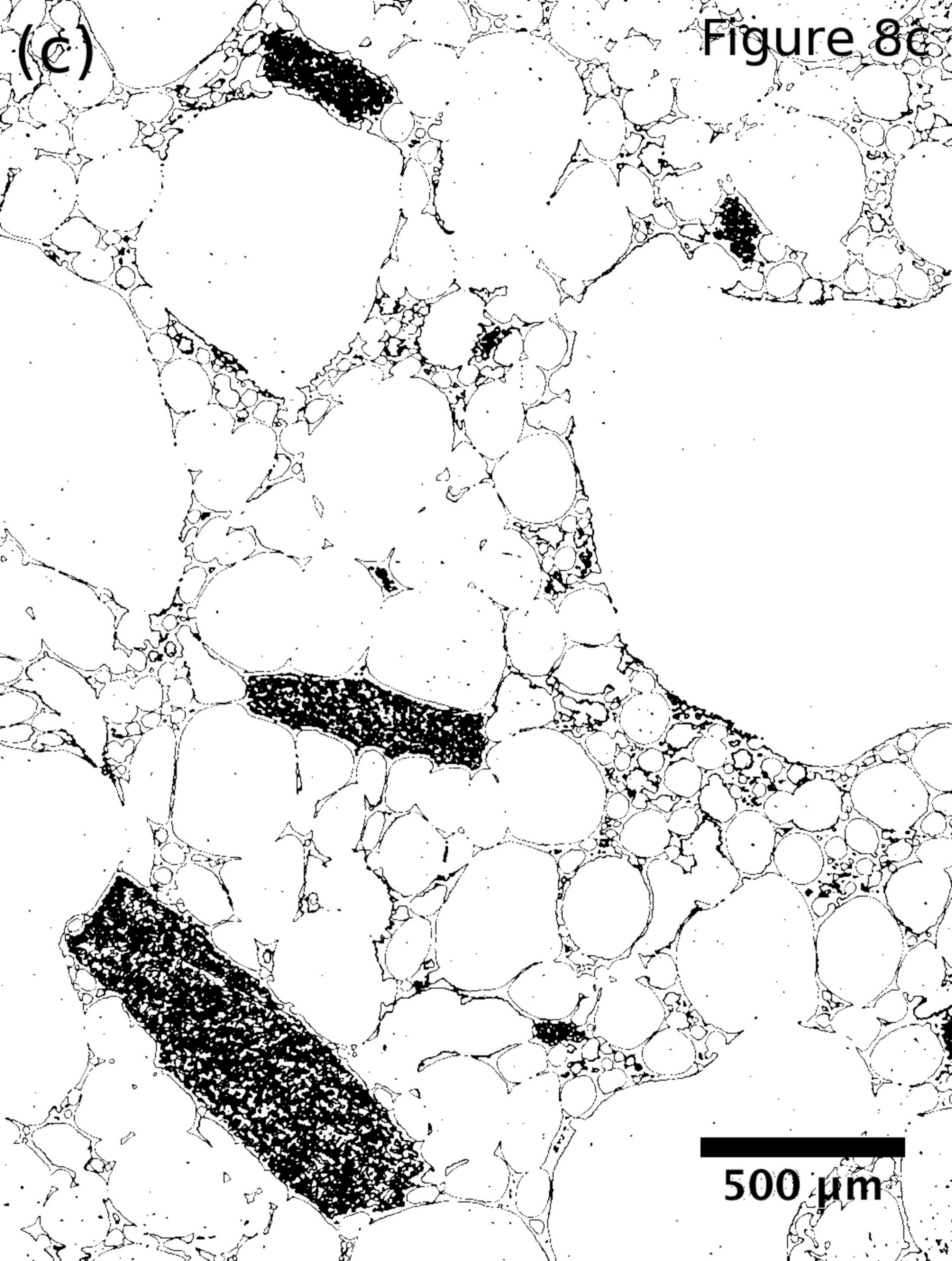(b)   Figure 8b

500 μm

(c)

Figure 8c

500 μm

(d)

Figure 8d

500 μm
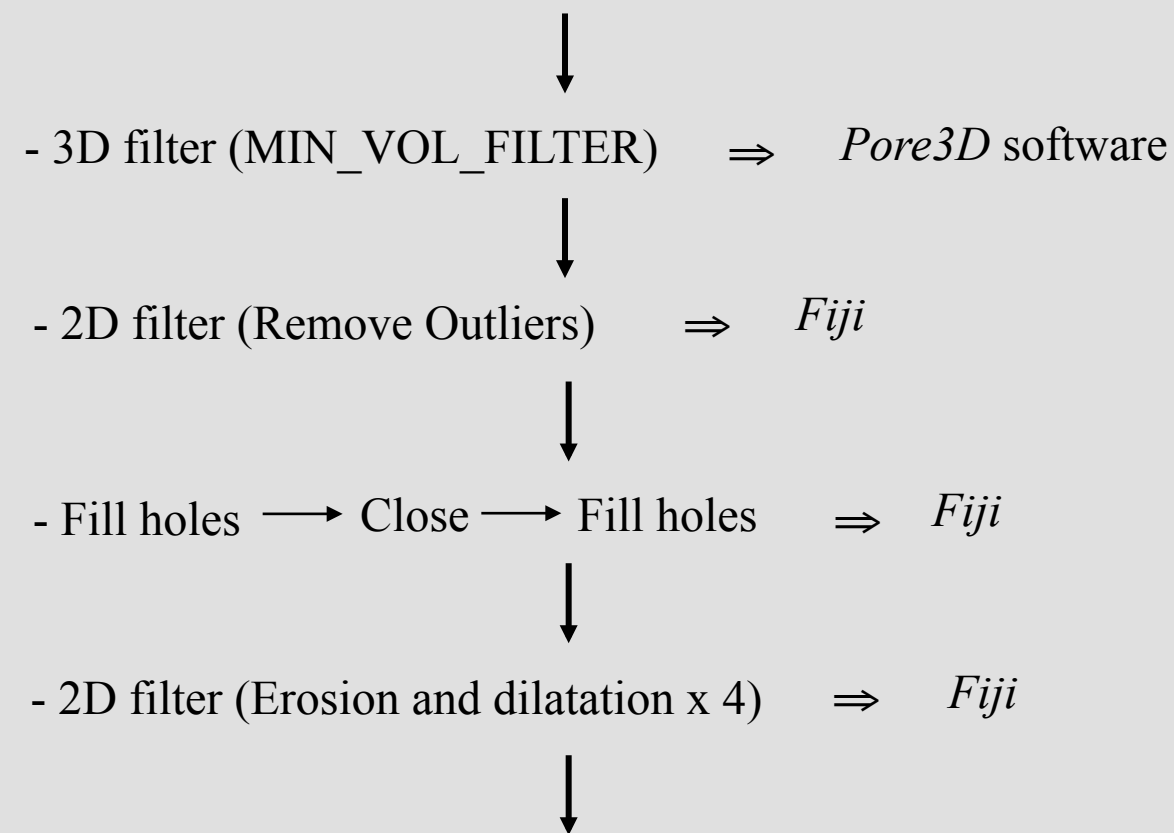
(e)

Figure 8e

500 μm

Figure 9

Segmentation with masking procedure

Manual thresholding

- **segmentation** of the real shape of plagioclase crystals taking into account a significant amount of pixel outliers, belonging to both vesicles and glass matrix that were not segmented after thresholding (Fig. 8b). We used the phase-retrieved raw volume (Fig. 8a) to segment plagioclase crystals. *Pore3D* software was used for the manual thresholding.

Mask preparation

- **segmentation** consisted in the approximate isolation of the shape of plagioclase (not necessarily the real shape) trying to take into account the smallest amount of pixel outliers possible (Fig. 8c). *Pore3D* software was used for the manual thresholding. We used the phase-retrieved raw volume (Fig. 8a) for mask preparation.

- 3D filter (MIN_VOL_FILTER) ⟹ *Pore3D* software

- 2D filter (Remove Outliers) ⟹ *Fiji*

- Fill holes ⟶ Close ⟶ Fill holes ⟹ *Fiji*

- 2D filter (Erosion and dilatation x 4) ⟹ *Fiji*

Mask of plagioclase crystals (Fig. 8d) is obtained from masking procedure

AND operator in *Fiji*

- Combine both the first segmentation (Fig. 8b) and the mask of plagioclase crystals (Fig. 8d) in order to complete the separation of the phase of interest.

- Plagioclase crystals were completely segmented preserving their shapes and internal structures (Fig. 8e)

(a)

Figure 10a

(b)

Scene
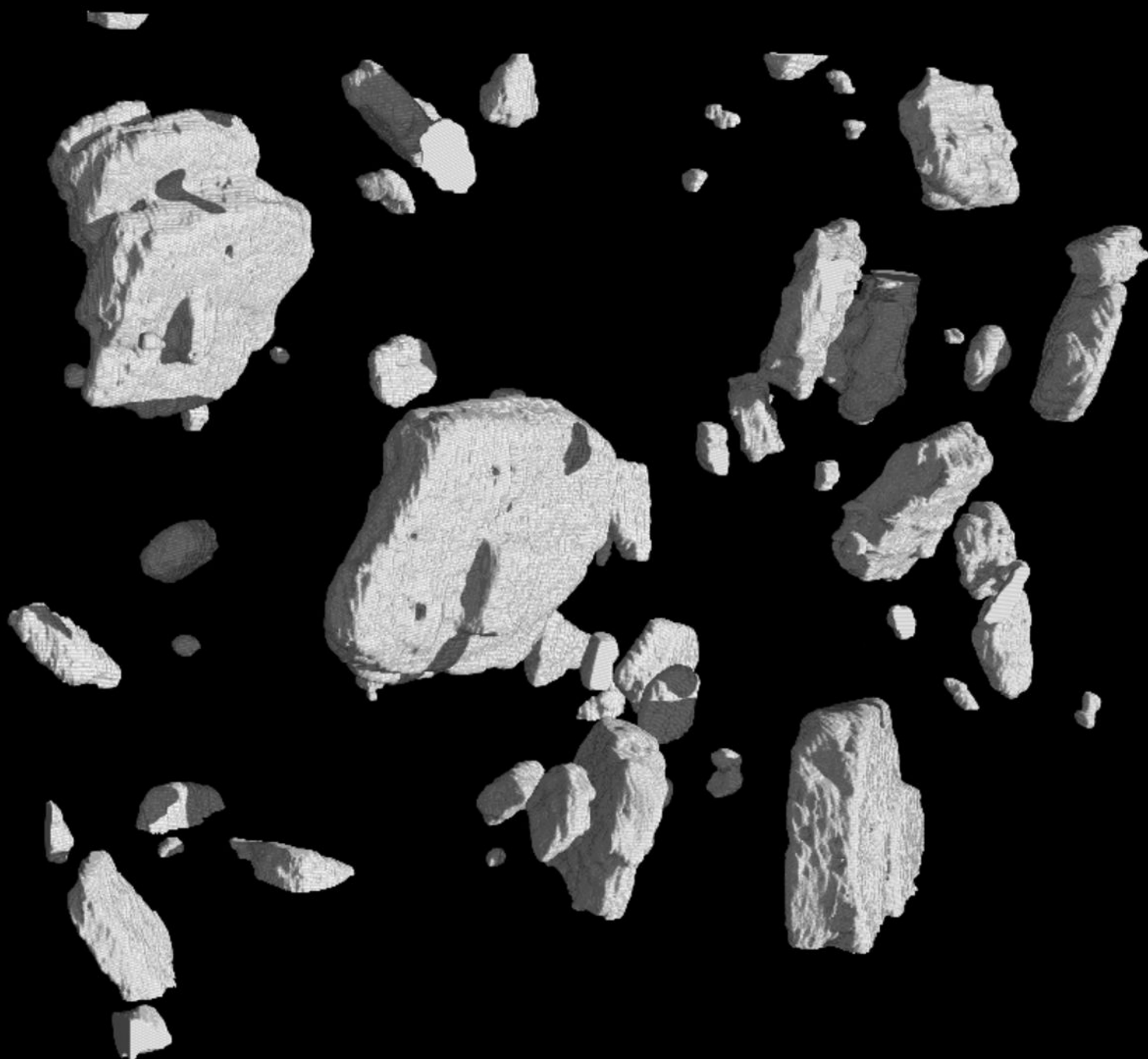
Figure 10b

1 Table 1. Summary of acquisition conditions and image processing details of the analysed
2 Volumes of Interest (VOI) for the investigated samples.

Sample	Instrument	Isotropic voxel size (µm)	Imaged volume (pixels)	Imaged volume (mm^3)	Analysed VOI (pixels)	Analysed VOI (mm^3)
ST16424119 8B	SYRMEP	2.2	1200x1400x1200	21.47	1056x1398x1000	15.72
D1	SYRMEP	2.0	-	3.95	-	3.95

3 note: ST164241198B is the nutural pumice of Stromboli. D1 is the trachytic synthetic sample.